SYNERGY OF MULTIPLE CYLINDERS IN FLOW INDUCED MOTION FOR HYDROKINETIC ENERGY HARNESSING

by

Eun Soo Kim

A dissertation submitted in partial fulfillment
of the requirements for the degree of
Doctor of Philosophy
(Mechanical Engineering)
in The University of Michigan
2013

Doctoral Committee:

Professor Michael M. Bernitsas, Chair
Associate Professor Luis P. Bernal
Professor Noel Perkins
Professor Nickolas Vlahopoulos

To my parents

Jung Moon Kim and Yeo Ja Lee

ACKNOWLEDGEMENTS

This dissertation is the result of the dedication and enthusiasm of all people who have shared in my life.

My deepest gratitude is to my advisor, Professor Michael M Bernitsas, for his guidance, support, and encouragement to do a Ph.D and complete this dissertation. Without his knowledge and wisdom, I would not have been able to complete this important stage of my life. I would like to thank my committee members, Professor Luis P. Bernal, Professor Noel Perkins, and Professor Nickolas Vlahopoulos. Their advice and critical comments were important to improve and complete my research.

I wish to express my sincere gratitude to Professor Steven L. Ceccio, for his help and advice on my Ph.D study.

I appreciate Eun Jung Chae, Che-Chun (Jim) Chang, Dae-Hyun Kim, Ayoung Kim, and Hongrae Park. Their support and care helped me overcome difficult times and complete my graduate studies.

I am also thankful to Mr. Jeff Drushal, Mr. Kent Pruss, and, Mr. David Carter who helped me build the new VIVACE oscillators and the new water channel. Without their efforts and help, this research would have not been finished. The most important of all, I wish to express my sincere gratitude and love to my family, my parents, my sister, Yeon woo Kim, and my brother-in-law, Judong Lee. They always believed in me and gave me their unconditional love.

I dedicate this dissertation to my father who suddenly passed away in 2009.

The following support is gratefully acknowledged: (1) DOE contract DE-EE0003644 to Vortex Hydro Energy with subcontract to the University of Michigan, (2) ONR grant N00014-10-1-0814 to the University of Michigan, Program Manager Kelly Copper, is gratefully acknowledged. (3) NSF-SBIR grant to Vortex Hydro Energy and the University of Michigan award #IIP-0810426, Program Manager William Haynes. (4) MUCI - Michigan University Commercialization Initiative, Program Manager Andrew McColm, 2009.

TABLE OF CONTENTS

LIST OF FIGURES

Figure

LIST OF TABLES

Table

ABSTRACT

SYNERGY OF MULTIPLE CYLINDERS IN FLOW INDUCED MOTION FOR HYDROKINETIC ENERGY HARNESSING

by

Eun Soo Kim

Chair: Professor Michael M. Bernitsas

Vortex Induced Vibrations for Aquatic Clean Energy (VIVACE) Converter is a converter of marine hydro-kinetic energy invented in the Marine Renewable Energy Lab (MRELab) and patented by the University of Michigan. It harnesses hydrokinetic energy from ocean/tidal/river currents. In its simplest form the VIVACE Converter is a single circular cylinder on springs with a power take-off system. Using passive turbulence control, VIVACE maximizes and utilizes flow induced motion in the form of vortex induced vibration or interference/proximity/wake/soft/hard galloping. MRELab has achieved back-to-back vortex induced vibration and galloping for a single cylinder with passive turbulence control thus more than doubling the range of synchronization of flow induced motion.

The goal of this research is to maximize the synergy of multiple cylinders in flow induced motion for hydrokinetic energy harnessing in order to increase the power volume density. In order to achieve this goal, the effects of tandem spacing, staggering, passive turbulence control, mass ratio, spring stiffness, damping, and number of cylinders in flow induced motion of multiple cylinders are studied experimentally. For these

experimental studies, two different generations of VIVACE converters were designed and built, and at the same time the old Low Turbulent Free Surface Water (LTFSW) Channel was replaced by the new LTFSW Channel. All model tests were conducted at high Reynolds numbers in the range of 28,000≤Re≤120,000, which primarily covers the TrSL2 and TrSL3 flow regimes. The following observations and conclusions are drawn: (a) By introducing PTC, all cylinders (2,3,4 tandem configurations) achieve galloping increasing the range of FIM synchronization with high amplitudes (2.2-3.49D) regardless of other parameters. (b) For tandem spacing of 1.43D, FIM of two cylinders in tandem is distinct: galloping starts earlier, amplitude is higher for the 2^{nd} cylinder, oscillation frequency is lower for both cylinders, and energy conversion is 60% higher. (c) For two cylinders in close tandem proximity (d/D<2.0), contrary to single cylinder studies, energy envelope points in galloping may not correspond to the highest spring stiffness (d) Higher mass ratio (m^*) results in higher marine hydro-kinetic energy conversion in galloping with practically no change in the VIV region. Increase by a factor of 2.5 was measured for 0.65<m^*<1.66. (e) Multiple cylinders in tandem can be in synergistic FIM in close proximity of d/D<2.0. (f) 2, 3, and 4 cylinders in synergistic FIM can harness more marine hydro-kinetic energy than the sum of the energy harnessed by each cylinder acting in isolation.

CHAPTER I

INTRODUCTION

1.1 Motivation

Global energy need has been growing fast as a result of industrial development and population growth. Global energy demand increased 45% between 1990 and 2010 (IEA, 2012). The report of the International Energy Agency (IEA) projects that global energy demands will be 35% higher in 2035 compared to 2010 in the New Policies Scenario. In particular, demand for electricity is the largest and fastest growing source of global energy demand. Electricity generation accounted for more than 35% of the primary energy consumption on a daily basis in 2010 and demand for electricity is projected to increase over 70% between 2010 and 2035. As a result, energy demand to generate electricity is expected to account for more than 40% of global energy demand in 2035. Moreover, the public is concerned more about global climate changes due to CO_2 emissions and safety issues after the Fukushima Daiichi nuclear power station incident in Japan. These concerns have led many countries to increase their use of renewable energy resources. According to IEA (2012) renewables, including hydropower, supplied 4,206TWh of electricity in 2010, which accounted for 20% of the world electricity generation in the same year. In the New Policies Scenario of IEA (2012), electricity from renewables is projected to increase 270% between 2010 and 2035. As a result, renewables are expected to deliver 11,342TWh of electricity

in 2035 and the share of renewables in global electricity generation would be more than 30%. In order to meet the projected electricity demands from renewable energy sources, however, traditional renewables such as hydro, wind and sun power would be insufficient to meet the projection and new types of renewable energy sources such as ocean energy resources should be utilized more to generate electricity.

Recently, many attempts to utilize the ocean energy resources to generate power have been made. Vortex Induced Vibration for Aquatic Clean Energy Converter (VIVACE) is a new concept to generate clean renewable electricity from ocean currents. VIVACE is a hydrokinetic power generating device invented by Bernitsas and Raghavan in 2005 and further developed by Bernitsas and his research group in the Marine Renewable Energy Lab (MRELab) of the University of Michigan (Bernitsas and Raghavan, 2009; Bernitsas, Ben-Simon, 2009; Lee and Bernitsas, 2011; Lee et al., 2011; Raghavan and Bernitsas, 2011; Chang et al., 2011, Chang and Bernitsas, 2011). Lee (2010) reported that a single cylinder (D=3.5", L=36") VIVACE Converter successfully generated hydrokinetic power from a current as slow as 0.4m/s and a maximum power of 15.85W at flow speed of 1.11m/s. Moreover, Chang (2010) was able to harness 49.35W at the flow speed of 1.45 m/s and the power volume density was 341W/m^3 at the flow speed of 1.45 m/s by utilizing Passive Turbulence Control (PTC) on the single cylinder VIVACE.

In light of the previous studies with a single cylinder VIVACE, it is reasonable to expect that if the single cylinder VIVACE successfully generated power from the current, multi-cylinder VIVACE converter could work synergistically, and thereby harness more power and increase the power volume density. In this dissertation, two different generations of multiple-cylinders VIVACE are designed, built, and tested in two different water channels. In order to prove the hypothesis, the response of multiple cylinders in Flow Induced Motions (FIM) are studied experimentally with variable parameters such as the number of cylinders, longitudinal and vertical spacing,

positions of PTC, spring stiffness, mass ratio, and Reynolds number.

1.2 Ocean Energy Technology

The oceans, lakes, and rivers cover more than 70% of the Earth's surface. Ocean resources in the form of tidal, wave, thermal gradient, and salt gradient have a substantial amount of potential energy as shown in Table 1.1. Nevertheless, the ocean renewables are not being fully utilized to generate electricity compared to their potential power resources. Only 1TWh out of 4,206TWh of global electricity generation from all types of renewables came from the ocean renewables in 2010 (IEA, 2012). IEA projects that electricity from ocean renewables will reach up to 57TWh by 2035, which is only 0.056% of the estimated potential global ocean power resources.

Table 1.1: Estimated ocean power resources (EPRI: Hydrokinetic and Wave Energy Technologies Workshop, Oct 26-428, 2005, WDC)

Form of Ocean Energy	Estimated Global Power Resource (TWh/yr)
Tidal	22,000
Waves	18,000
Thermal gradient	2,000,000
Salt gradient	23,000
Total	2,063,000

The low contribution of the ocean renewables on the world electricity generation is because most of the present ocean renewable power technologies have not been successfully commercialized as yet due to the low efficiency and high cost of power generation compared to the traditional fossil fuels, or even solar and wind powers (U.S. Department of Energy (DOE), 2009; International Renewable Energy Agency (IREA), 2012). Interest in ocean renewables is, however, increasing and many different ocean technologies are being developed for commercialization.

1.2.1 Wave energy technology

Wave energy technologies generally utilize the motion of a device either floating on the ocean surface or moored on the seabed. The wave energy technologies are the most commercially advanced in ocean energy conversion (DOE, 2009). The followings are examples of the present ocean wave converters.

A) Point absorbers (Figure 1.1)

The point absorbers usually have a small floating part whose surface area is very small in comparison to the wavelength of the ocean waves.

(i) Archimedes Wave Swing (AWS)

:Source-AWS Ocean Energy Ltd., www.awsocean.com

This technology was invented by a Scottish company, AWS Ocean Energy Ltd. The AWS is a fully submerged (50∼150m) air-filled piston that expands and contracts in response to wave pressures. Relative movement between the moving and stationary parts drives a hydraulic system and the kinetic energy is converted to electricity by means of a linear generator. A 2MW prototype was first tested at full scale offshore in Portugal in October, 2004 and delivered power at predicted levels of 250kW. A 1:9 scale model of AWS-III was also tested on Loch Ness in 2010 to get a design data. A 10MW pre-commercial demonstration farm is planned to be operated in 2014.

(ii) PowerBuoy (Figure 1.2)

: Source-OceanPowerTechnology, www.oceanpowertechnologies.com

The PowerBuoy was developed in 1985 by Ocean Power Technologies (OPT) and was first tested in 1997 in New Jersey. Moreover, it has received the first Federal approval among ocean renewable technologies to build a commercial wave farm in the US. This moored buoy moves up and down with

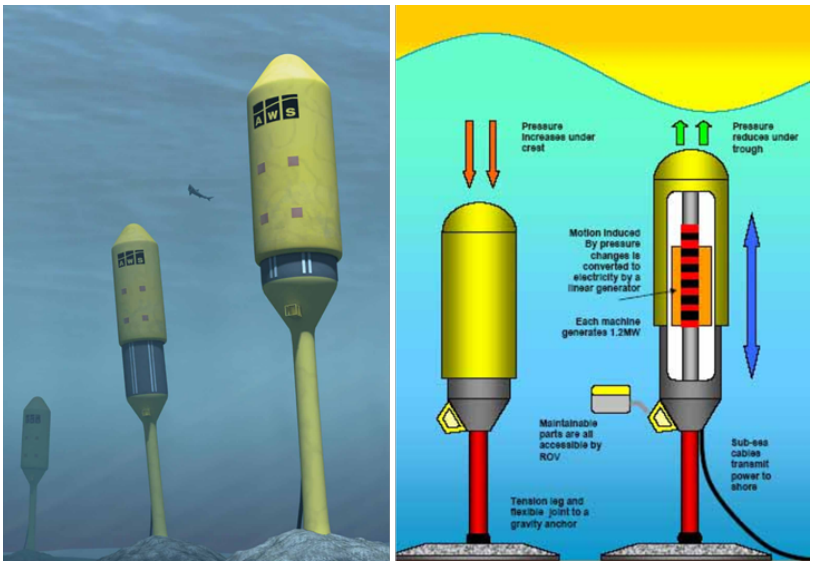

Figure 1.1: Schematic of AWS [Reproduced from www.awsocean.com]

waves and the resultant mechanical stoking is converted into electricity by a power take off system. The first 1MW wave park was deployed for the U.S. Navy in Oahu, Hawaii from 2009 to 2011. A commercial prototype of OPT's PowerBuoy was deployed off the coast of Invergordon in Scotland. Other commercial wave park projects are in progress in Oregon, the North coast of Spain and Victoria, Australia.

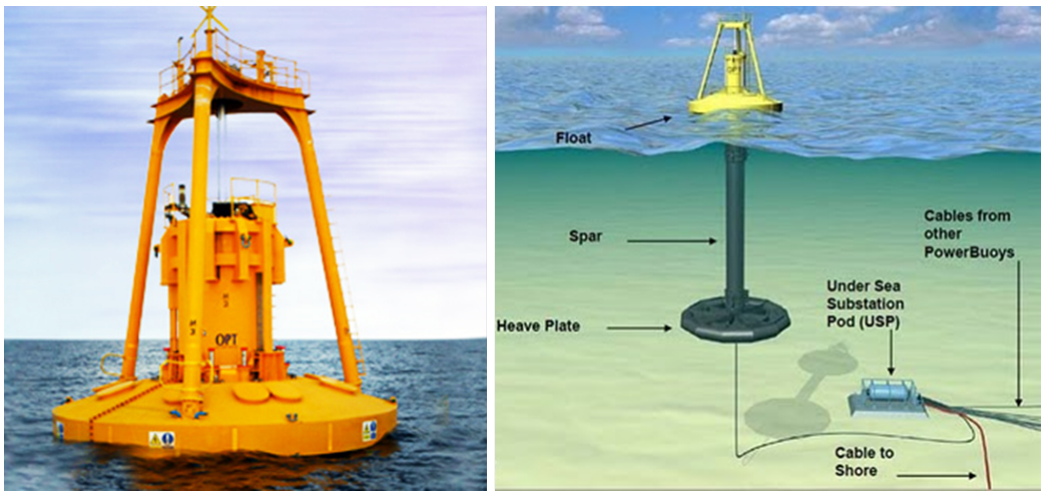

Figure 1.2: Prototype deployed in 2011 (left) and schematicb (right) of the PowerBuoy [Reproduced from www.oceanpowertechnologies.com]

(iii) Aquabuoy (Figure 1.3)

: Source-Finavera Renewables Inc., http://finavera.com/

Aquabuoy was first created by Technocean, in the early 1980's during the Swedish Wave Energy Program. A moored buoy floats on the ocean surface and moves up and down as a result of the motion of the waves. The motion of the buoy drives a piston in a vertical tube below the water that then drives a hose pump. The hose pump pressurizes seawater inside and the seawater drives the Pelton. The first test was conducted in 1981 outside Götenborg in the open sea. The first large prototype was deployed off the coast of Oregon in September 2007 and was rated for up to 250kW. The Pacific Gas and Electric Company signed purchasing agreement of a 2MW wave power at a site off the shore of Humboldt, California in 2007 and planned to generate power at the site in 2012.

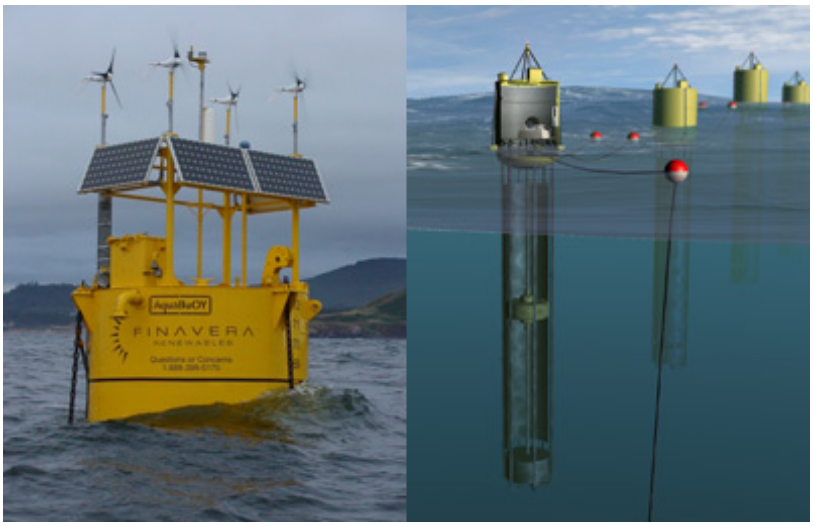

Figure 1.3: Full scale prototype deployed in 2007 (left) schematic (right) of the Aquabuoy [Reproduced from http://finavera.com]

B) Attenuator (Figure 1.4)

Attenuators have relatively long buoyant segments compared to the ocean wavelengths, and are oriented parallel to the general direction of wave propagation

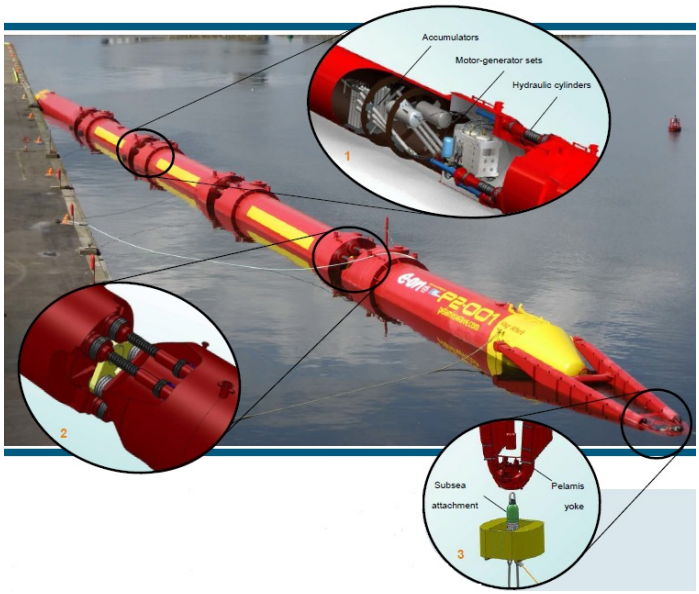

Figure 1.4: The second generation of full scale prototype and schematic of the Pelamis [Reproduced from www.pelamiswave.com]

(i) Pelamis

: Source-Pelamis Wave Power, www.pelamiswave.com

The Pelamis project began in 1998, and the first test of the device was conducted at the European Marine Energy Center (EMEC) in 2004. Pelamis consists of four semi-submerged tubes hinged by hydraulic joints. Three ram pumps placed at each joint resist wave motion and convert the relative articulation of each tube into hydraulic pressure. The high pressure pumps oil through hydraulic motors that drive twin 125kW generators to produce electricity. The second generation of the Pelamis (P2) is 180m long, 4m diameter, and approximately 1350 tons in weight. The Pelamis P2 was first installed off the west coast of the Orkney mainland in October 2010 to test the machine through various sea conditions for three years. Currently, a 10MW Pelamis farm off the southwest coast of Shetland is in development.

C) Terminator (Figure 1.5)

This type of the wave energy converters is oriented perpendicular to the wave crests, and absorbs a large amount of the energy content of incident waves. The device consists of a stationary part fixed to the sea floor, and a part moving with the waves. The moving part pressurizes a fluid to drive a turbine.

(i) Oscillating Water Column (OWC)

: Source-Oceanlinx, www.oceanlinx.com

OWC was first developed in 1992 by Oceanlinx (previously Energetech), and its first prototype was tested in 1997. The device has two openings: one opening is submerged under water to allow water to enter in and evacuate from the column as the waves pass, and the water pushes and pulls the air inside through the other opening. The turbine is driven by the moving air. A full scale prototype was operated between 2005 and 2009 to collect data that guided the development of subsequent designs. The pre-commercial demonstration scale device was deployed and operated for three months at Port Kembia in 2010, and it provided grid quality power to integral energy.

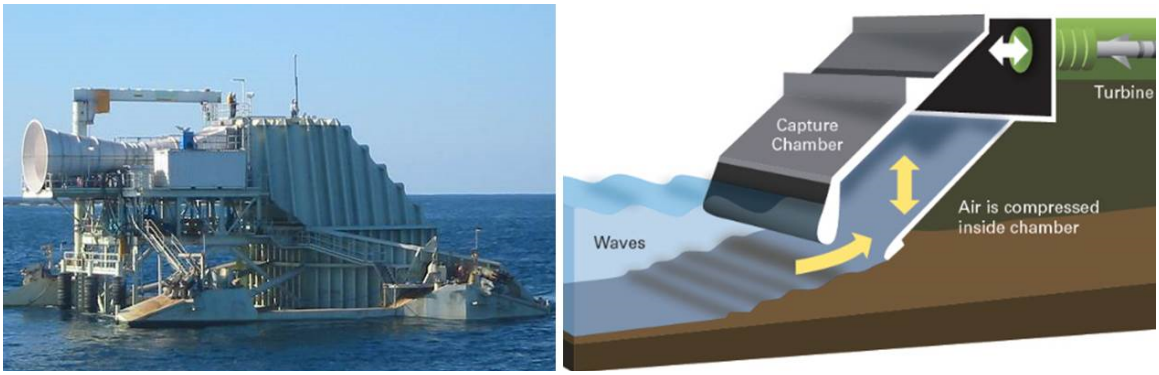

Figure 1.5: Full scale prototype deployed in 2005 (left) and schematic (right) of the OWC [Reproduced from www.oceanlinx.com]

(ii) Oyster (Figure 1.6)

: Source-Aquamarine Power: www.aquamarinepower.com

The Oyster wave power technology was invented in 2001 by Professor Trevor Whittaker's research team at Queen's University. This device was designed to capture energy in near shore waves and convert it to electricity. It consists of a hinged buoyant flap that oscillates with the motion of the waves, and a power connector frame fixed on the seabed. The oscillation of the flap drives hydraulic pumps that push pressurized water to drive an onshore hydroelectric generator. The first full scale prototype was built in 2007 and installed at the EMEC in Orkney in 2009. The next generation of the Oyster was installed and delivered electricity to the grid in June 2012. The device is 26m wide and is installed at a depth of around 13m. It has a maximum generating capacity of 800kW.

Figure 1.6: Full scale prototype installed in Orkney (left) and schematic of the Oyster [Reproduced from www.aquamarinepower.com]

1.2.2 Ocean thermal technology

The Ocean thermal energy conversion (OTEC) utilizes the thermal gradient between warm surface seawater and cold deep water to generate electricity (Roas and Vieira, 2009; DOE, 2009). The OTEC technology was first developed in 1881 by a

French physicist, and the first test plant was built and delivered 22kW of electricity in Matanzas, Cuba in 1930 (Takahashi et al., 1991). A 210kW open cycle OTEC experimental apparatus successfully operated at the Natural Energy Laboratory of Hawaii (NELH) in 1993 (Vega, 1993). OTEC technologies can be categorized into two types of a closed cycle system and open cycle system based on the heat cycles. Both designs use the Rankin cycle with a low-pressure turbine. The closed system uses a working fluid, such as ammonia or R-134a, which has a low boiling point. The ammonia is vaporized in the first heat exchanger by warm surface seawater and powers the low-pressure turbine to generate electricity. The ammonia passed through the turbine is pumped through the second heat exchanger to be condensed into a liquid by the cold deep water, and then the liquid ammonia is recirculated through the system. The open cycle system uses the seawater directly as a working fluid to generate power. The warm seawater is pumped into a low-pressure chamber and it is converted to steam, which drives the turbine. The steam passes through a heat exchanger filled with cold deep water, and then it is converted into fresh water. In the open cycle system, the by-products of desalinized fresh water remain after the seawater is circulated in the cycle and this fresh water can be used for drinking water.

Makai Ocean Engineering constructed an OTEC Heat Exchanger Test Facility at the NELH in 2011 to collect data for the optimal design of an OTEC plant. Recently, Lockheed Martin has announced that a plan for a 10MW OTEC power plant off the coast of southern China is in progress and it will be designed by the company.

1.2.3 Ocean current technology

Ocean currents are the third largest source among ocean renewables. Ocean current energy technologies capture the hydro kinetic energy and convert it to electricity. Most ocean current converters are turbines, submerged in seawater similar to small

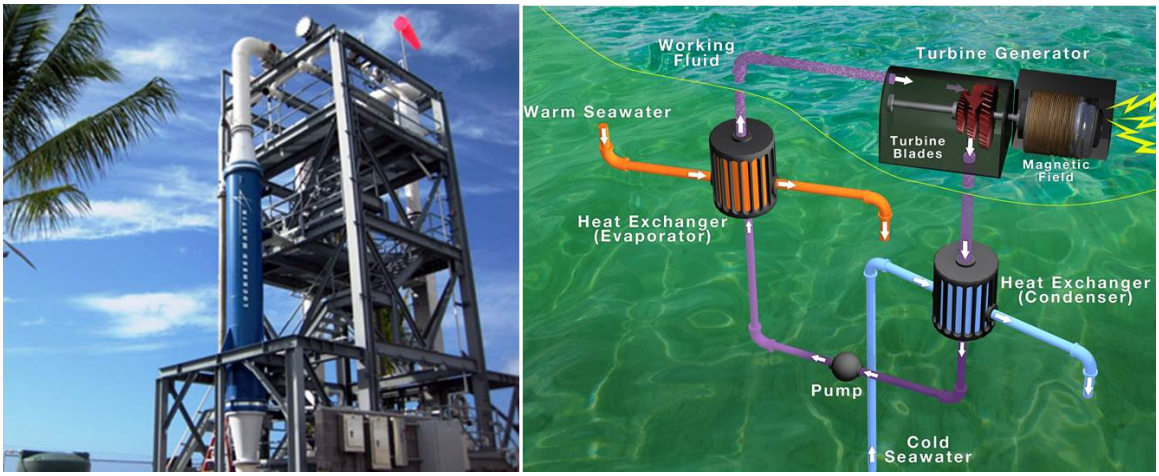

Figure 1.7: Lockheed Martin's OTEC Test facility in Hawaii (left) and schematic of the OTEC (right) [Reproduced from www.lockheedmartin.com]

wind turbines. The followings are examples of ocean turbines.

A) SeaGen (Figure 1.8)

: Source-Sea Generation Ltd., www.seageneration.co.uk

The SeaGen which is designed by the Marine Current Turbine Ltd (MCT) is an open rotor type of the marine current turbine. The marine currents drive two submerged blades that are designed to operate in bi-axial flows by being pitched 180 degrees. The first 300kW prototype, which was installed in May 2003 off the coast of Devon, UK, is still operating today. A 1.2MW pre-commercial prototype with 18m long blades was deployed for the test in Northern Ireland in April 2008, and it has been licensed to operate for 5 years. A 10MW power project off the coast of Anglesey is also in progress, and nine SeaGen devices are expected to be deployed in 2014 and will operate for 25 years. The MCT expects to deliver electricity to the grid in 2015.

B) Tidal Turbine (Figure 1.9)

Figure 1.8: 1.2M Test prototype installed in 2008 (left) and schematic of the SeaGen [Reproduced from www.seageneration.co.uk]

: Source-Clean Current Power System Inc., http://www.cleancurrent.com

Clean Current's Tidal Turbine is a shrouded rotor type that is housed in a symmetrical tapered duct. The bi-directional blades rotate by marine currents and the duct was designed to enhance turbine performance in turbulent and off-axis flows. This turbine is designed to be operated in both river and ocean currents. The first 65kW demonstration turbine was installed at Race Rocks, British Columbia in September 2006 and it was tested for 9 months. The power output of 65kW was rated at the current speed of 3.0m/s. Clean Current Power System provides many different sizes of tidal turbines from 65kW to 500kW based on the rated power output at the 3.0m/s current speed. The company is planning to deploy their first commercial river turbine in Manitoba, Canada in 2013.

1.2.4 Tidal technology

Tidal energy technologies utilize the potential energy caused by difference in sea levels due to the gravitational force of the moon. Conventional tidal energy technology

Figure 1.9: Demonstration Prototype installed in 2006 and schematic of Tidal Turbine [Reproduced from www.cleancurrent.com]

works similar to a dam. They consist of a huge barrage to retain water during high tide and a hydro turbine, which generates power when the water runs through it during low tide. Barrages raise environmental concerns such as blocking navigation and impeding fish migration (DOE, 2009). However, there is a new attempt to generate power from the tide by using a low-head hydroelectric system, which is called Tidal Lagoons patented by Tidal Electric Inc (source: Tidal Electric Inc.). Tidal lagoons replace the barrage by an impoundment wall that is expected to resolve the previous environmental considerations. The low-head hydroelectric generation system consists of a mixed-flow reversible bulb turbine, a generator, and a control system. The mechanism to generate power is the same as the one for the barrage type technology.

Three projects are in progress in Wales: 30MW in Swansea Bay, 30MW in Fifoots Point, and 432MW in North Wales. The design life for the Tidal Lagoons is over 100 years. Tidal Electric expects to deliver electricity to the National Grid in 2017. The company has been granted funding from the China government to support for a 300MW project in China's coastal water.

As previously seen, many ocean renewable technologies have been developed and

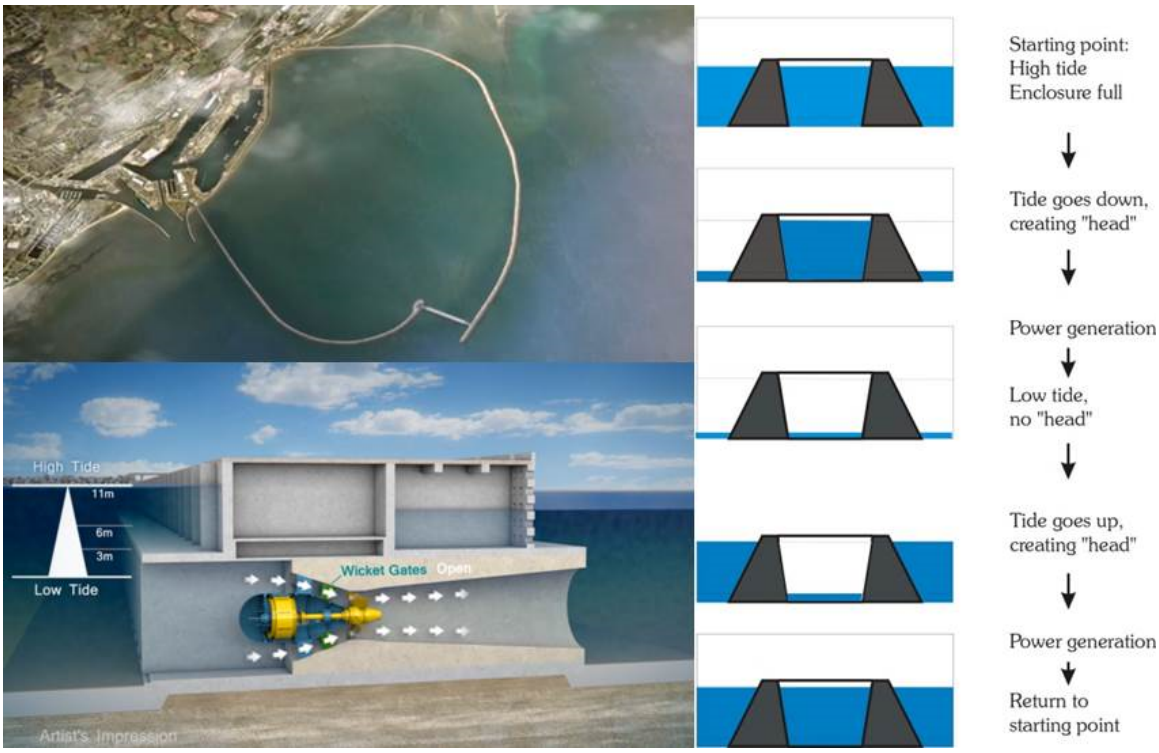

Figure 1.10: Aeroview of Swansea Bay's Tidal Lagoon (left) and schematic of the Tidal Lagoon (right) [Reproduced from www.tidalelectric.com]

patented in recent years. However, there are still some challenges for the technologies to overcome before they become commercially viable. First, one of the major challenges is variation of ocean weather conditions. Particularly, for the wave energy technology, the wave energy converters are generally designed to function in a certain range of the wave frequencies, and the energy conversion efficiency drops when the converters run at wave conditions below or above the design conditions. Moreover, severe weather conditions, such as storms, can cause significant structural damage, and these harsh conditions can shorten the design lift of the converters.

The second obstacle is the limited number of locations where these technologies can be used. Seagen functions well only in excess of 2.4m/s (4.7knots) of tidal current (Marine Current Turbine Ltd.), and Clean Current's Tidal Turbines can produce only rated power in the current speeds of greater than 2.6m/s (5knots) (Clean Current

Power System Inc.) while the majority of currents on the earth are slower than 3knots. For the OTEC, at least a temperature difference of 20° C (36°F) is required to generate usable power, so the installation locations are limited to equatorial regions (DOE, 2009). Additionally, there are only about 20 locations on the earth where power from the tide can be generated because the difference in height between high tide and low tide must be greater than 5m to capture sufficient power (DOE, 2009).

Another challenge is the grid connection. Most of the devices are deployed offshore, and generated power should be transmitted to onshore power grids. The installation and maintenance of power cables under the oceans are still challenging, and increase costs as well.

The environmental impacts of the technology deployments are not yet known, and thus long-term studies are required.

Many researchers have been trying to overcome these drawbacks and to utilize more ocean renewables to generate power efficiently. In this dissertation, Vortex Induced Vibration Aquatic Clean Energy (VIVACE) Converter which is a novel idea to generate power from ocean or river currents is introduced in next section.

1.3 Single Cylinder VIVACE Converter

Unlike previous efforts to suppress the occurrence of Flow Induced Motions (FIM), which is a potential destructive phenomenon for structures subjected in a fluid flow, VIVACE enhances and utilizes FIM to harness power from river and ocean currents. The first prototype of VIVACE was developed in late 2003, and tested in the MRELab in 2004. The first field tests were conducted in September 2010.

Vortex-Induced Vibration (VIV) is one of the best-known FIMs, which is induced on bluff bodies such as circular cylinders exposed to a fluid flow perpendicular to the cylinder axis. Boundary layers separate from the surface on either side of the body, giving rise to a broad wake behind it where the free shear layers (separated

boundary layers) roll and form vortices. These vortices are alternatively shed from either side of the body, altering the pressure distribution causing periodic forces to act on the cylinder leading to VIV, which is named lock-in or synchronization. For decades, researchers have been working on how to eliminate or at least regulate this unsteady fluid-structure interaction phenomenon since it has been identified as the cause for many structural failures. Unlike previous efforts to suppress the occurrence of this phenomenon, VIVACE works on enhancing VIV to maximize it and convert its mechanical energy extracted from the fluid flow into electric power.

The simplest form of the VIVACE Converter, shown in Figure 1.11, is a single smooth cylinder suspended by springs with a Power-Take-Off (PTO) system.

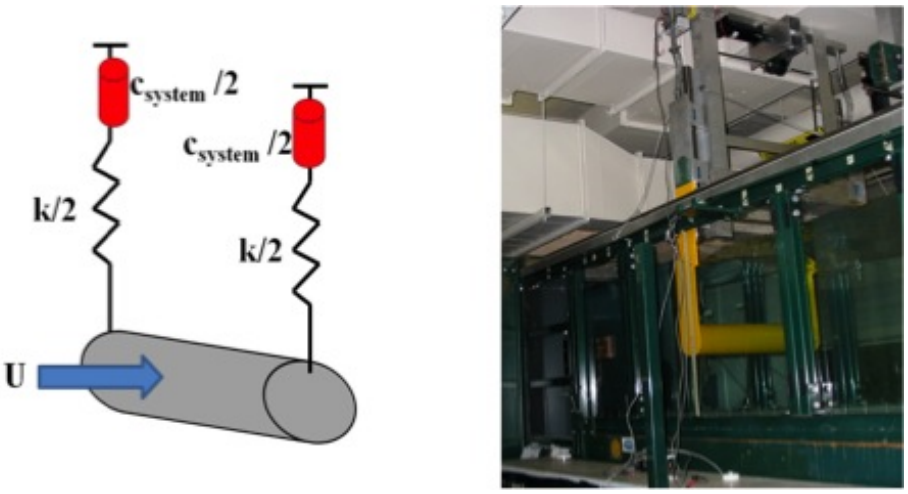

Figure 1.11: Schematic of a single-cylinder VIVACE (left) and the 1^{st} generation of lab prototype (right)

Extensive tests on Vortex Induced Vibration (VIV) were performed to harness optimal power at various current speeds with the single-cylinder VIVACE for Reynolds number 40,000<Re<120,000 and various damping and spring stiffness in the MRE-Lab (Lee and Bernitsas, 2011). All single cylinder tests presented here were done in the Low Turbulence Free Surface Water (LTFSW) Channel in MRELab with a circular cross-section of diameter D=3.5" in length L=36" in length. A virtual

spring-damping (Vck) system, which is a servomotor-controller mechanism to replace physical dampers and springs, was designed and built by Lee et al.(2011) for investigating the effect of damping and spring stiffness on generating power. They produced an optimal VIVACE power envelop in Figure 1.12. Figure 1.12 shows that VIVACE can generate hydrokinetic power from a current as slow as 0.4m/s and a maximum power of 15.85W at the flow speed of 1.11m/s with K=1,800N/m and $\zeta_{harness}$ =0.12. Initially, the VIVACE Converter was supposed to utilize only VIV, as implied in its name. Due to the self-limiting nature of VIV, harnessed power from a single-cylinder VIVACE Converter was constrained by the lock-in range and self-limiting oscillating amplitude of VIV. Some previous studies, however, on FIM of circular cylinders bring to light the fact that a fluid dynamic change brought about by virtue of attachments may cause galloping in circular cylinders (Bernitsas and Raghavan, 2007a; Raghavan and Bernitsas, 2008; Chang et al., 2011). In contrast to VIV, where the amplitudes are self-limiting, galloping is known to be a single degree of freedom, high amplitude, low frequency oscillation typically experienced by non-circular cross-sectional bodies (Alonso, 2009). Galloping is basically caused by induction of negative aerodynamic/hydrodynamic damping by which the total system damping falls below zero thereby generating motion-aiding forces producing very high amplitude motions. In an attempt to overcome VIV's drawbacks and initiate galloping for the VIVACE cylinder, the MRELab research team has extensively investigated effects of roughness strips, which act as Passive Turbulence Control (PTC), on FIMs of a circular cylinder (Chang et al., 2011; Park et al., 2011).

The studies show that selectively applied roughness could cause substantial changes in the characteristics of the boundary layer or the shear layers and thereby the cylinder response. For some selected circumferential locations of the roughness strips, as shown in Figure 1.13, PTC expands the VIV upper branch to $U^*\approx$11 and initiates fully developed galloping around $U^*\approx$12. There is a transition range where both VIV

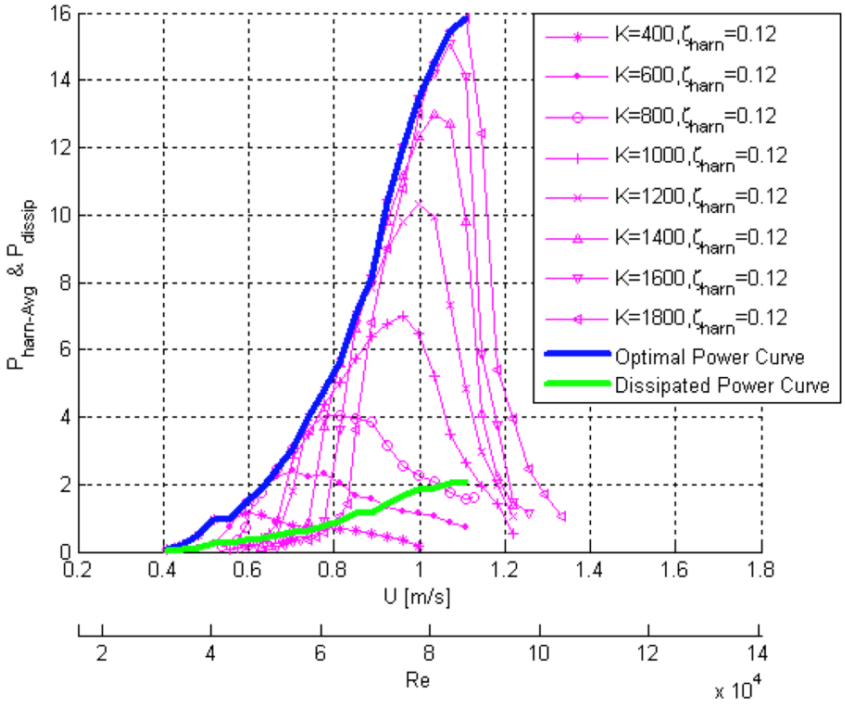

Figure 7-10. Optimal Power Envelop and Corresponding Dissipated Power

Figure 1.12: Optimal power envelop and corresponding disspated power of a single-cylinder VIVACE [Reproduced from Lee, 2010]

and galloping mechanisms coexist $11<U^{*}<12$. Thus, the FIM range of synchronization, which encompasses back-to-back VIV and galloping, increases dramatically.

As a result, the VIVACE was enabled to harness higher power over a broader range of velocity from 0.38m/s to 1.45m/s, the maximum running speed of the Low Turbulence Free Surface Water (LTFSW) Channel of MRELab. Superposing the result of calculated harness power with different combinations of damping and spring stiffness values, the optimal harnessed power curve is generated and is shown in Figure 1.14 (Chang, 2010). The optimal harnessed power of the cylinder with PTC is greater than that of the smooth cylinder in the region of VIV synchronization. Moreover, the harness power curve dramatically starts to jump up once the flow speed is greater than 1.2m/s and reaches 49.35W at the flow speed of 1.45m/s for K=2,000N/m, $\zeta_{harness}$=0.16 while the smooth cylinder cannot harness power any

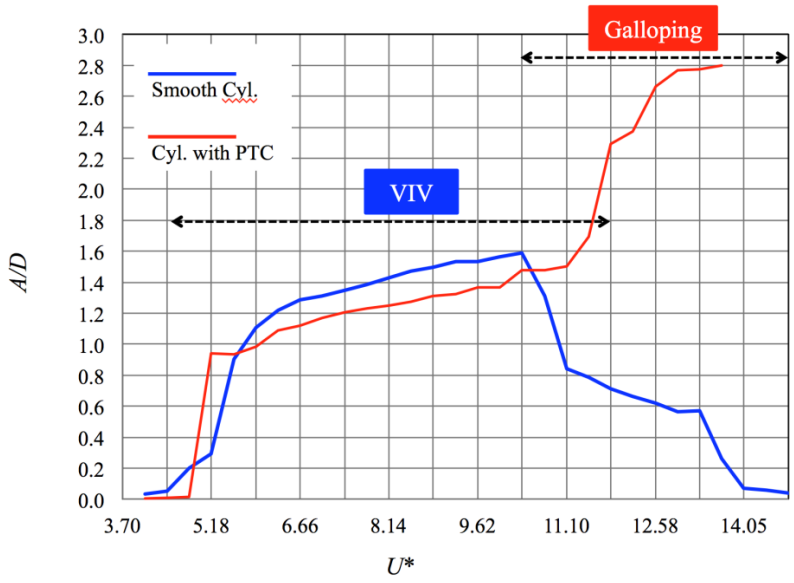

Figure 1.13: FIM zone nomenclature for a circular cylinder with PTC

more due to de-synchronization. The power calculated at 1.45m/s is more than three times the maximum harnessed power of a smooth cylinder. Due to the limitation of the facilities, the tests could not be done at speeds higher than 1.45m/s.

Power volume density is one of the important criteria used to compare the efficiency of energy converters. Chang (2010) estimated the power volume density of the single-cylinder VIVACE based on the test results. For estimation of power volume density, a staggered configuration with the center-to-center spacing of $8D$ in the streamwise direction and $5D$ in the transverse direction was selected, as shown in Figure 1.15 These spacings are well above the minimum required distance to minimize the interference between cylinders (Zdravkovich, 1997). The portion of two cylinders was included in the selected volume, and then the power volume density was calculated as follows, where P_{harn} is the harnessed power.

For the selected configuration of the cylinder deployment, the maximum power density 300.73W/m^3 was reported at the flow speed of 1.38m/s. The flow speed of 1.38m/s is the water speed corresponding to the rated wind speed of 13m/s. By

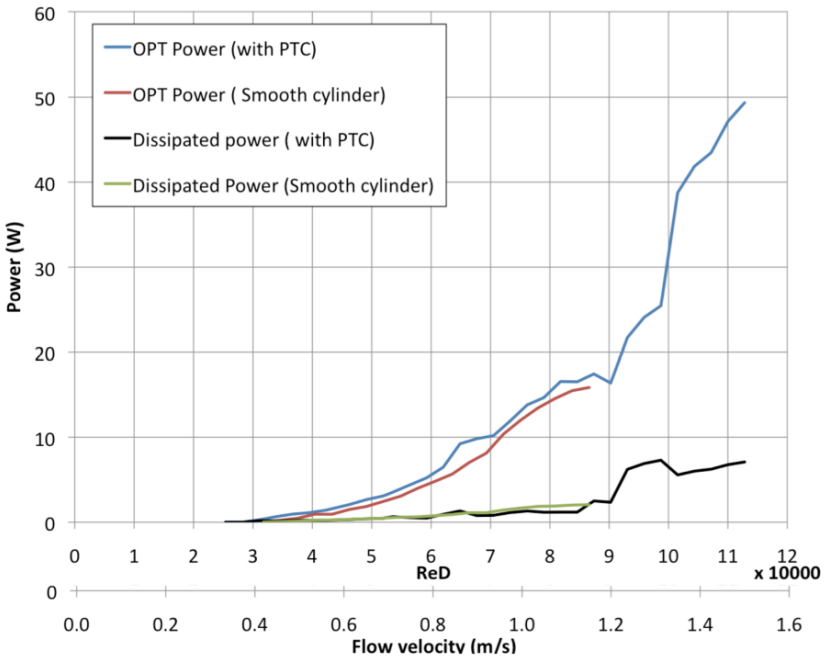

Figure 8.19. Optimal harnessed power envelope of VIVACE with PTC and without PTC.

Figure 1.14: Optimal harnessed power envelope of VIVACE with PTC and without PTC [Reproduced from Chang, 2010]

considering the availability of current and the efficiency of a generator that requires a gearbox, the power density drops by 223.74W/m^3. However, the estimated power volume density was much higher compared to the power density of 0.0046W/m^3 of the Roscoe wind farm, the largest wind farm in the world in 2010.

1.4 Scope of the Dissertation

The single cylinder VIVACE Converter harnessed hydrokinetic energy from currents as slow as 2knots while the lowest operating flow speed limit of watermills/turbines is 4knots with 5−7knots being the required speed for their financial viability. The vast majority of flow currents are slower than 3knots and typical rivers are slower than 2knots. The harnessed power from a single VIVACE module developed in MRELab is about 50W at a flow speed of 1.45 m/s which is the top speed used in the LTFSW Channel (Chang, 2010). All the previous studies on VIVACE (Bernitsas et al., 2009;

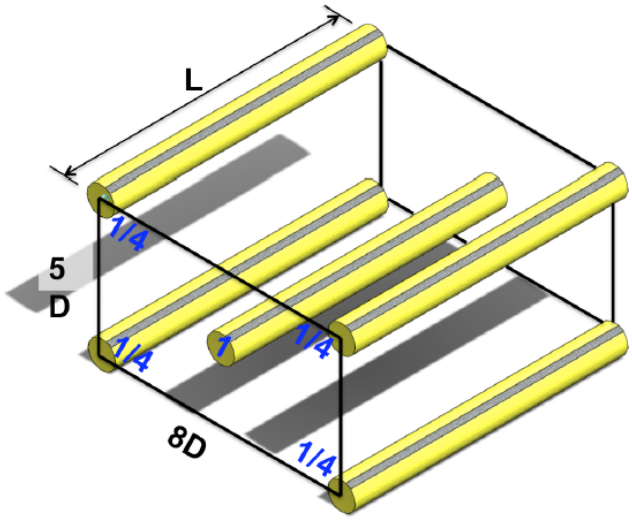

Figure 1.15: Configuration of cylinder deployment of the VIVACE

Lee and Bernitsas, 2011; Lee et al., 2011; Raghavan and Bernitsas, 2008, 2011; Chang et al., 2011; Park et al., 2011) were conducted with only a single cylinder with various values spring stiffness, damping, and PTC.

The goal of this dissertation is to maximize the synergy of multiple cylinders in FIM for hydrokinetic energy harnessing. In order to achieve this goal, the following studies are needed,

(a) To understand the effects of center-to-center spacing on multiple cylinders in FIM

(b) To understand the effects of staggering on FIM of multiple cylinders

(c) To understand the effects of PTC on FIM of multiple cylinders

(d) To understand the effects of mass ratio on FIM of multiple cylinders

(e) To understand the effects of spring stiffness on FIM of multiple cylinders

(f) To understand the effects of above parameters on energy harnessing

To investigate the effects of those parameters, two new lab scale prototypes of the VIVACE were designed, built and tested in MRELab. All tests presented in Part A of this dissertation were conducted with the 2^{nd} generation of VIVACE in the LTFSW Channel. The LTFSW Channel was replaced by a new one built in April 2012. In Part B, the 3^{rd} generation of prototype is introduced. The flow calibration of the new LTFSW Channel results are presented in Chapter 8. All the tests presented in Part B have been done with the 3^{rd} generation of VIVACE in the new LTFSW Channel. It should be emphasized that this dissertation, apart from revealing the dynamics of cylinders in multi-cylinder configurations, has a far-reaching impact on the development of the VIVACE Converter towards becoming a unique three-dimensional energy absorber similar to a school of fish. This should be contrasted to point absorbers (buoys), line absorbers (Pelamis), area absorbers (watermills / turbines), or surface absorbers (oscillating water columns).

This dissertation is organized as follows:

PART A. ENHANCEMENT OF SYNERGISTIC FLUID INDUCED MOTION OF MULTIPLE CIRCULAR CYLINDERS

Chapter1. INTRODUCTION

Chapter2. LITERATURE REVIEW

Chapter3. EXPERIMENTAL SETUP

Chapter4. FLOW INDUCED MOTION OF MULTIPLE CYLINDERS

PART B. OPTIMAL DESIGN OF MUlTI-CYLINDER VIVACE CONVERTER TO MAXIMIZE HARNESSED POWER

Chapter5. DESIGN OF NEW VIVACE CONVERTER

Chapter6. MEASUREMENT OF VELOCITY DISTRIBUTION OF NEW LOW TURBULENCE FREE SURFACE WATER CHANNEL

CHAPTER II

LITERATURE REVIEW

2.1 Vortex Induced Vibration

Flow-Induced Motion (FIM) is a phenomenon that frequently occurs when slender structures are subjected to a transverse fluid flow. The most commonly encountered FIM phenomenon is Vortex-Induced Vibration (VIV). VIV of a single cylinder has been studied by numerous researchers over the eight decades and is comprehensively summarized in the recent reviews of Sarpkaya (2004), Williamson and Govardhan (2004), Bearman (2011), and Xu et al. (2012).

An elastically mounted rigid cylinder is free to oscillate only transversly to the flow, and as the flow speed increases vortices are formed behind the cylinder, and shed one side of the cylinder at a time, alternating between the two sides. This vortex shedding alters the pressure distribution causing periodic lift forces to act on the cylinders. The large oscillations of the cylinder occur when the shedding frequency is synchronized with the oscillation frequency. Unlike resonance of a linear system, this synchronization occurs over a range of frequencies, is called synchronization or lock-in (Sarpkaya, 1995; Williamson and Govardhan, 2004). Based on the amplitude response, Khalak and Williamson (1996, 1997a,b, 1999) classified the VIV regimes into three branches as shown in Figure 2.1: the initial branch, upper branch, and lower branch They showed that the transition between the initial and upper branches

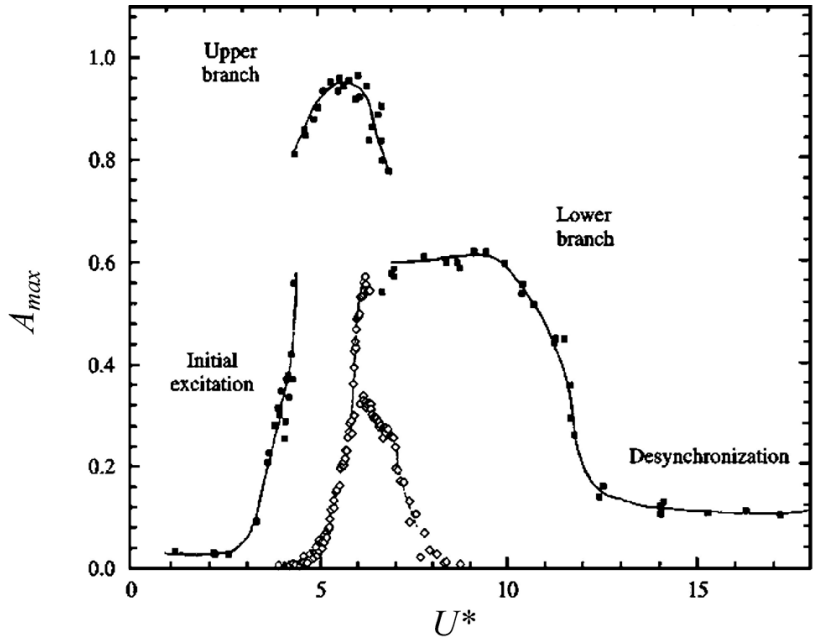

Figure 2.1: Classification of the VIV branches based on the amplitude responses [Reproduced from Khalak and Williamson, 1999]

is a hysteresis while the shift from the upper to lower branch is intermittent. Prior to this observation, Williamson and Roshoko (1988) demonstrated that different vortex shedding modes are associated with specific VIV regimes as shown in Figure 2.2. The vortex modes are classified by the number of vortices shed per cycle and their grouping as illustrated in Figure 2.2. The designations 2S, 2P, and P+S indicate two single vortices, two pair vortices, and one pair and one singe vortices shedding per cycle, respectively. The 2S mode occurs in the initial branch and the 2P mode is associated with the lower branch. The shift from the lower branch to initial branch corresponds to the change in the vortex shedding mode with a phase shift in the lift forces (Govardhan and Williamson, 2000).

The vortex shedding frequency is another important feature of the VIV and is generally represented by the Strouhal number (St) which is a nondimensional number and defined as St= $f_v D/U$. The f_v is the vortex shedding frequency. For a stationary cylinder, the St is almost constant with a value of 0.2 for Reynolds numbers from 100 to 10^5(White, 2006) while for an oscillating cylinder, it deviates from the value

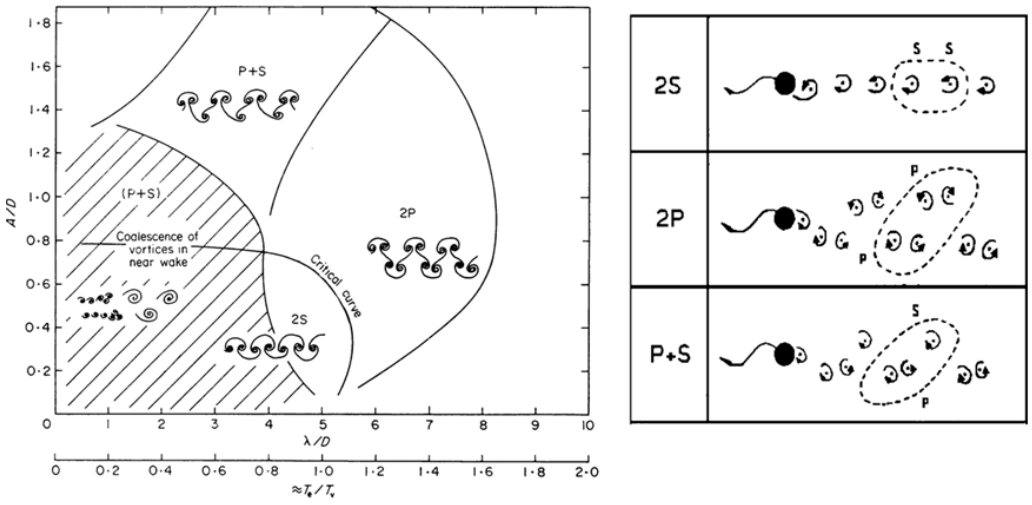

Figure 2.2: The map of regimes for vortex wake modes (left) and schematic of vortex formation modes (right) [Reproduced form William and Roshoko, 1988]

of 0.2 as the oscillatory amplitude increases. The deviation increases with increase in the mass ratio, which is the ratio of the mass of all the oscillating parts to the displaced fluid mass due to the volume of the parts as shown in Figure 2.3. One can find further features of VIV in the comprehensive reviews mentioned earlier in this section. In this dissertation, VIV in groups of multiple circular cylinders will be investigated experimentally.

2.2 Galloping

Galloping is a self-excited vibration, with one degree of freedom instability characterized by a large amplitude and a low frequency motion. VIV is driven by the exciting force caused by alternating vortex shedding, so the amplitude is self-limited while the oscillatory amplitude of galloping keeps increasing until the system fails due to the nature of the instability. Galloping is caused by the coupling between the fluid forces and the oscillation of a body submerged in the flow. As the body oscillates transversely to the flow, the angle of attack of the incident flow periodically changes, which causes the oscillating fluid forces on the body, and the body thereby becomes

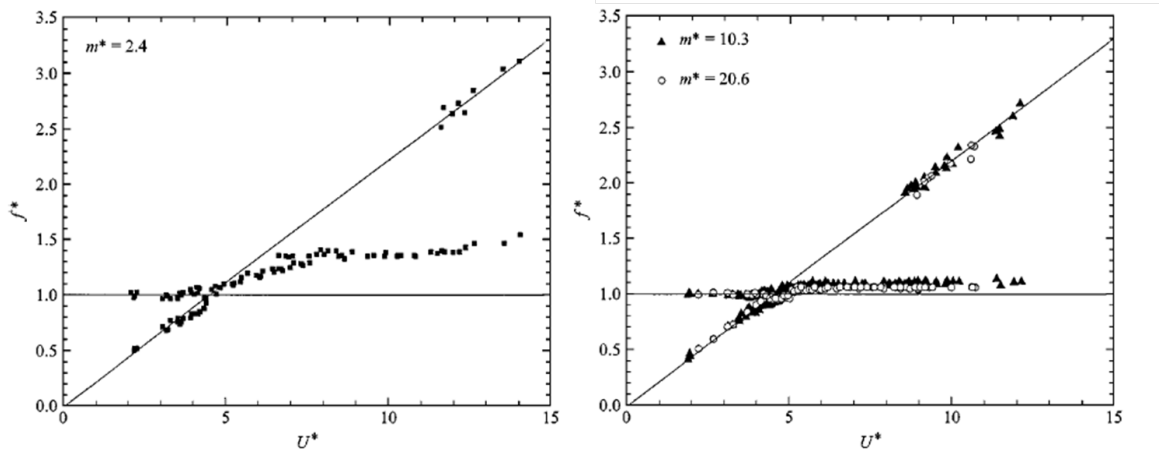

Figure 2.3: Frequency response for a range of mass ratios through the synchronization regime [Reproduced from Khalak and Williamson, 1999]

dynamically unstable, potentially resulting in large amplitude oscillations due to the oscillating fluid forces (Blevins,1990). This instability is generally explained as a consequence of the fluid damping, which usually dissipates energy from the system. The fluid forces, which are caused by the motion of a body in a fluid, can be decomposed in an acceleration dependent inertial force and a velocity-square dependent drag force (Morison et al. 1950, Sarpkaya 1978). The drag force term introduces an additional damping in the oscillating system, and the total damping of the system is the sum of this fluid damping and the structural damping. The force caused by the structural damping is always opposite to the direction of the body motion, and dissipates energy from the system. The fluid damping force, however, can be either in phase or out of phase with the body motion. If the fluid damping force in phase with the body motion is greater than the structural damping, the total damping becomes negative, and the system is thereby unstable and experiences galloping.

The initiation of galloping depends on many factors such as cross sectional geometry, angle of incident flow, free stream velocity, mechanical properties of the mass, structural damping, and spring stiffness. It is known that a long slender body with only a non-circular cross section experiences galloping, and a smooth cylinder can-

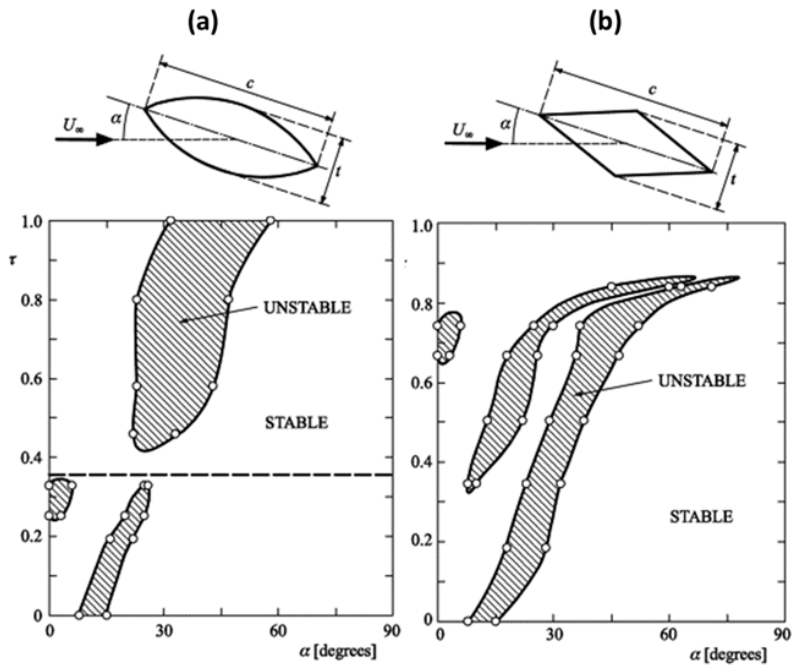

Figure 2.4: Stability diagram in the angle of attack (α)-aspect ratio ($\tau = t/c$) plane, based on static test results: (a) Rhomboidal cross section bodies, and (b) biconvex cross section bodies [Reproduced from Alonso et al., 2009]

not gallop due to its symmetric geometry (Alonso et al., 2009). Alonso et al. (2005, 2007, 2009) investigated the effects of the cross section geometry and angle of incident flow. They used three different types of cross sectional cylinders: triangular, biconvex and rhomboidal, and found unstable conditions based on static test results. Their experimental studies demonstrated that galloping is highly dependent on the cross sectional geometry and angle of incident flow as shown in Figure 2.4. Kazahevich and Vasilenko (1996) analytically studied the galloping instability to determine the critical free stream velocity for the initiation of galloping, which is given as,

$$U_{cr} = \frac{2U^3}{A^2\omega_n^2}\left(\sqrt{1+\frac{A^2\omega_n^2}{U^2}}-1\right) \tag{2.1}$$

where A, U, and ω_n are the oscillatory amplitude, free stream velocity, and natural frequency of the system, respectively. Using Eqn. (2.1), they expected that one could determine the critical free stream velocity by only a single experimental result having

one experimental point in the parameters of A, U, and ω_n.

By introducing Passive Turbulence Control (PTC) , which is a roughness strip, Bernitsas and his research team (Chang et al., 2011; Park et al., 2011; 2012) showed experimentally that a circular cross sectional cylinder can also experience galloping. They have broadly investigated the effect of PTC. By introducing PTC, they were able to achieve back-to-back VIV and galloping of a single circular cylinder. The selectively applied roughness strips cause changes in the boundary or shear layers, and, in turn, changes in the response of cylinder oscillations. Moreover, PTC modifies the circular cross sectional geometry of the smooth cylinder, and fixes the separation point of the boundary layer, which increases the asymmetry of the flow structure. Park (2012), in particular, thoroughly investigated the effects of PTC on VIV and galloping of a circular cylinder, and produced the *PTC-to-FIM* Map based on the amplitude response of the cylinder as illustrated in Figure 2.5. He reported that the location of the PTC dramatically changes the amplitude response of the circular cylinder, and FIM can be either suppressed or enhanced based on the location of the PTC as shown in Figures 2.6 and 2.7. One of the goals of this dissertation is to enhance the FIM of multiple cylinders using the PTC to harness more of the hydrokinetic energy of the fluid flow. The effects of the PTC on the FIM of multiple cylinders is be experimentally investigated in this dissertation.

2.3 Mathematical Model for FIM of a Single Cylinder

The equation of motion for an oscillating cylinder in the transverse direction with linear springs and damping, $y(\mathrm{t})$, to a steady flow can be modeled as follows,

$$m_{osc}\ddot{y} + c_{sys}\dot{y} + Ky = F_{fluid,Total}(t) \tag{2.2}$$

where m_{osc}, c_{sys}, K, and $F_{fluid,Total}$ are the mass of the oscillating parts, struc-

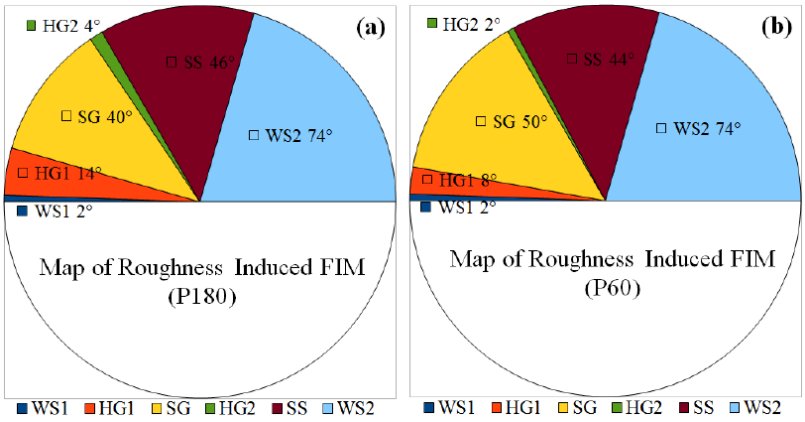

Figure 2.5: Map of the PTC to FIM: (a) P180 and (b)P60- Zone: Weak Suppression(WS), Strong Suppression(SS), Hard Galloping(HG), and Soft Galloping(SG) zones [Reproduced from Park et al., 2012]

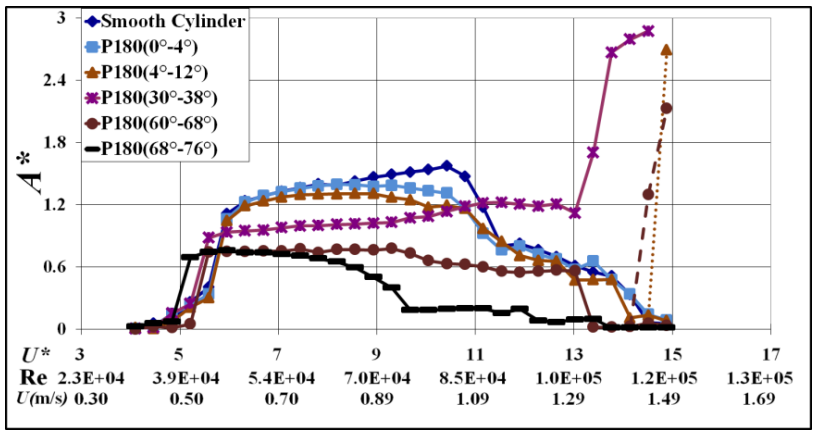

Figure 2.6: Effect of the location of the PTC (P180) on FIM of a circular cylinder [Reproduced from Park, 2012]

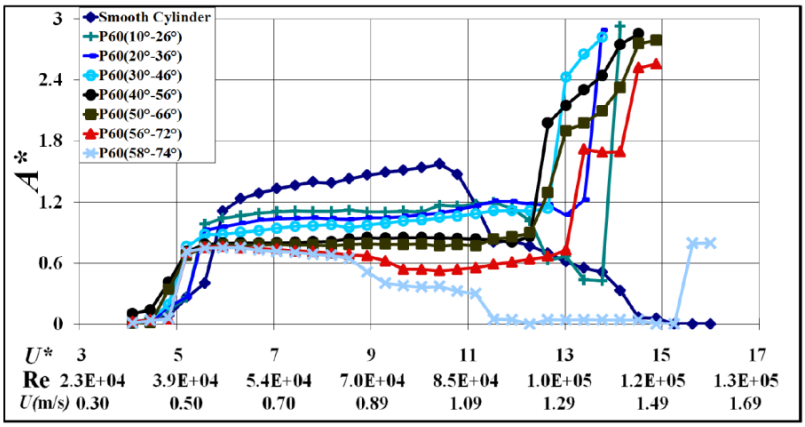

Figure 2.7: Effect of the location of the PTC (P60) on FIM of a circular cylinder [Reproduced from Park, 2012]

tural damping coefficient, spring stiffness, and time dependent total fluid force in the transverse direction. Mathematical modeling for the time dependent fluid force is challenging, and it is still being debated due to the complexity of the interaction between body dynamics and fluid dynamics.

One of the most commonly used models in offshore engineering is Morison types of the force decomposition, so named because this model of force decomposition was first suggested by Morison, O'Brien, Johnson, and Schaaf (1950), to estimate inline fluid forces acting on a cylindrical body in an oscillating flow. In Morison's model, the time dependent fluid force acting on a cylinder is assumed to be the linear sum of an acceleration-dependent inertial force and a velocity-square-dependent drag force. Accordingly, the time dependent fluid force is written as

$$F_{fluid,Total}(t) = C_m \rho \frac{\pi D^2 L}{4} \frac{\mathrm{d}U}{\mathrm{d}t} + \frac{1}{2} C_d \rho D L U |U| \tag{2.3}$$

where ρ, U, D, and L are the density of the fluid, free stream velocity, diameter, and length of the cylinder, respectively. C_m, and C_d, are the cycle-averaged inertia and drag coefficients. This force decomposition model is semi-empirical because C_m,, and C_d, should be experimentally determined, and they depend on the the Keulegan-Carpenter number (KC), which is a dimensionless number classifying the inertia and drag dominant regimes. Forces further depend on Re and surface roughness. Sarpkaya (1977, 1986) experimentally investigated the in-line and transverse forces acting on smooth and rough circular cylinders placed in oscillatory flow for Re up to 700,000 and presented comprehensive data on C_m,, and C_d in his papers. It is important to notice that the inertia and drag coefficients in Morison's model share the effect of the vorticity field. Accordingly in a vortex-dominated flow, prediction using Morison's approach is inaccurate. Lighthill (1986b) proposed that the inviscid inertia force and viscous drag force could operate independently, and thus the time dependent fluid force could be decomposed into two distinct components, which are: an inviscid

inertial force and a viscous drag force. Based on his proposal, he modified Morison's model as

$$F_{fluid,Total}(t) = C_m^* \rho \frac{\pi D^2 L}{4} \frac{\mathrm{d}U}{\mathrm{d}t} + \frac{1}{2} C_d \rho D L U |U| \tag{2.4}$$

where C_m^* is the added mass coefficient of the 'ideal inviscid' flow. In Lighthill's model, the inviscid inertia force doesn't account for the contribution of the vorticity field, and all the vortex-induce forces contribute only to the viscous drag force.

Govardhan and Williamson (2000) adopted Lihthill's force decomposition to describe the dynamic response of a single cylinder in VIV, and named the ideal inertia force and viscous drag force a potential force and a vortex force, respectively. Then, the fluid force can be expressed as

$$F_{fluid,Total}(t) = F_{POTENTIAL}(t) + F_{VORTEX}(t) \tag{2.5}$$

The potential force is given by

$$F_{POTENTIAL}(t) = -C_a \rho \frac{\pi D^2 L}{4} \ddot{y} = -m_a \ddot{y} \tag{2.6}$$

where $C_a (= C_m^*)$ and m_a are the added mass coefficient and added mass, respectively.

Goverdhan and Williamson introduced a vortex force coefficient and a vortex phase, ϕ_{vortex}. The latter is defined as the phase between vortex force and displacement, to describe the switching in the timing of vortex shedding caused by the shift in the vortex mode from 2S to 2P. With the substitution of the Eqns. (2.5) and (2.6) in the Eqn. (2.2), the equation of motion of a cylinder oscillating transversely to the flow can be written as

$$\left(m_{osc} + m_a\right) \ddot{y} + c_{sys} \dot{y} + K y = F_{VORTEX}(t) \tag{2.7}$$

By assuming a periodic fluid force, the vortex force is given by

$$F_{VORTEX}(t) = F_{VORTEX} \sin(2\pi f t + \phi_{vortex}) \tag{2.8}$$

and the dynamic response of the cylinder can be expressed by

$$y(t) = A \sin(2\pi f t) \tag{2.9}$$

where f is the oscillation frequency of the cylinder. In lock-in or synchronization, the oscillation frequency is equal to the vortex-mode shedding frequency.

Blevins (1990) also used the same force decomposition proposed by Lighthill (1986b) to explain the galloping instability of a spring-supported bluff body in a steady flow as shown in Figure 2.8. As previously discussed, the instability is caused by the aerodynamic or hydrodynamic forces which are in phase with the velocity of the body. He used a quasi-steady model for the aerodynamic force and then examined its response during small perturbations from the equilibrium state. Based on the quasi-steady assumption, the equation of motion for the bluff body is given by,

$$(m_{osc} + m_a)\,\ddot{y} + c_{sys}\dot{y} + Ky = \frac{1}{2} C_y \rho D L U^2 \tag{2.10}$$

Blevins used C_y instead of C_d which was used in Lighthill's model to indicate the direction of the force. The fluid force is not a function of time anymore.

The angle of attack is defined by

$$\alpha = \arctan\left(\frac{\dot{y}}{U}\right) \tag{2.11}$$

where U is the free stream velocity.

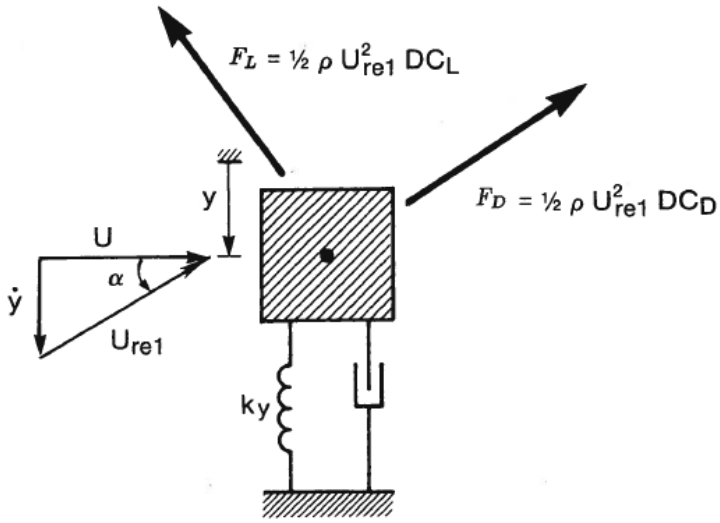

Figure 2.8: One degree of freedom galloping model [Reproduced from Blevins, 1990]

The relative velocity of flow to the moving body is given by

$$U_{rel}^2 = \dot{y}^2 + U^2 \tag{2.12}$$

Blevins decomposed the steady transverse fluid force into the lift force, which is perpendicular to the relative flow, and the drag force, which is parallel to the relative flow. The lift force and drag force are defined by

$$F_L = \frac{1}{2}\rho U^2 DLC_L \tag{2.13}$$

$$F_D = \frac{1}{2}\rho U^2 DLC_D \tag{2.14}$$

where C_L, and C_D, are the lift and drag coefficients, respectively.

By normalizing Eqns. (2.10), (2.13), and (2.14) by $1/2\rho U^2 DL$, the steady transverse force coefficient, C_y, is given by,

$$C_y = -\frac{U_{rel}^2}{U^2}\left(C_L \cos\alpha + C_D \sin\alpha\right) \tag{2.15}$$

C_y, C_L, and C_D depend on the geometry, angle of attack, and Re.

For small angles of attack, α, U_{rel},and C_y can be expressed in power series as follows

$$\alpha = \frac{\dot{y}}{U} + O(\alpha^2) \tag{2.16}$$

$$U_{rel} = U + O(\alpha^2) \tag{2.17}$$

$$C_y(\alpha) = C_y|_{\alpha=0} + \frac{\partial C_y}{\partial \alpha}\Big|_{\alpha=0} + O(\alpha^2) \tag{2.18}$$

By substituting Eqn. (2.12) in Eqns. (2.16)–(2.18), C_y can be rewritten s,

$$C_y(\alpha) = -C_L|_{\alpha=0} - \Big[\frac{\partial C_L}{\partial \alpha} + C_D\Big]_{\alpha=0} + O(\alpha^2) \tag{2.19}$$

$$\frac{\partial C_y}{\partial \alpha}\Big|_{\alpha=0} = -\Big[\frac{\partial C_L}{\partial \alpha} + C_D\Big]_{\alpha=0} \tag{2.20}$$

where $O(\alpha^2)$ means that the 2^{nd} and higher power terms are neglected.

By substituting Eqns. (2.10), (2.16), (2.17), (2.18), (2.19), and (2.20) in Eqn. (2.10), the equation of motion is becomes

$$\begin{aligned}(m_{osc} + m_a)\ddot{y} + c_{sys}\dot{y} + Ky \\ = \frac{1}{2}\rho U^2 DL\left[- C_L|_{\alpha=0} + \frac{\partial C_y}{\partial \alpha}\Big|_{\alpha=0}\left(\frac{\dot{y}}{U}\right)\right] + O(\alpha^2)\end{aligned} \tag{2.21}$$

Using the definition of the structural damping ratio and natural frequency, Eqn. (2.21)

can be rewritten as,

$$(m_{osc}+m_a)\left[\ddot{y}+2\omega_y\Big(\zeta_y-\frac{\rho UDL}{4(m_{osc}+m_a)\omega_y}\frac{\partial C_y}{\partial\alpha}\Big|_{\alpha=0}\Big)\dot{y}\right]+Ky$$
$$=-\frac{1}{2}\rho U^2 DLC_L|_{\alpha=0} \tag{2.22}$$

where

$$\zeta_y=\frac{C_{sys}}{2(m_{osc}+m_a)\omega_y},\quad \omega_y=\sqrt{\frac{K}{m_{osc}+m_a}} \tag{2.23}$$

Therefore, the total damping ratio (ζ_{Total}), which accounts for both structural damping and aero or hydro dynamic damping, can be defined as follows,

$$\zeta_{Total}=\zeta_y-\frac{\rho UDL}{4(m_{osc}+m_a)\omega_y}\frac{\partial C_y}{\partial\alpha}\bigg|_{\alpha=0} \tag{2.24}$$

The slope of vertical force coefficient, $\frac{\partial C_y}{\partial\alpha}\ |_{\alpha=0}$, is a function of the geometry and Re. The total damping ratio can be less than zero, if the following condition is satisfied.

$$\frac{\partial C_y}{\partial\alpha}\bigg|_{\alpha=0}\geq\frac{4(m_{osc}+m_a)\omega_y}{\rho UDL}\zeta_y,\ \text{or}\quad \left[\frac{\partial C_L}{\partial\alpha}+C_D\right]_{\alpha=0}\leq-\frac{4(m_{osc}+m_a)\omega_y}{\rho UDL}\zeta_y \tag{2.25}$$

For this condition, the system becomes unstable and galloping can be initiated. As discussed earlier, Govardhan and Williamson (2000), and Blevins (1990) adopted Lighthill's model (1986b) to describe the time dependent fluid force. In Lighthill's model, the time dependent fluid force is decomposed into the inviscid inertial force and the viscous drag force which are assumed to operate independently. Leonard and Roshko (2001) numerically studied VIV of a circular cylinder oscillating transversely in a tow-dimensional flow at Re=100, and the results of numerical simulation, which uses Lighthill's force decomposition model, were in good agreement with the exper-

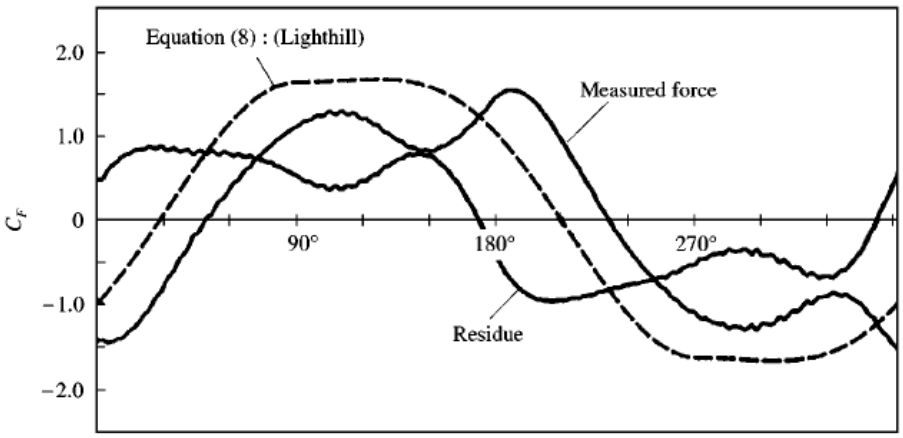

Figure 2.9: Normalized measured force, force calculated using Lighthill's model, and the residue=calculated force-measured force [Reproduced from Sarpkaya, 2001]

imental data. Williamson (2004) presented this result as a proof of the validity of Lighthill's force decomposition model.

However, Sarpkaya (2001) reached a contrary result. He measured the time dependent force for a sinusoidally oscillating flow about a circular cylinder, and compared the data with the force calculated using Lighthill's model as shown in Figure 2.9. From this comparison, he concluded that the inviscid inertia force and the viscous drag force do not operate independently, and thus Lighthill's force decomposition model is invalid. He further concluded that the creation, convection, and diffusion of vorticity contribute to both the inertia force and viscous drag force, and the added mass coefficient (or inertia coefficient) changes with time during a given cycle.

As previously noted, it is still difficult to theoretically describe the time dependent fluid forces exerted on an oscillating body because their nature is highly nonlinear.

2.4 Flow Induced Motion of Multiple Cylinders

Vortex induced vibration of a single cylinder, which has been studied for several decades, is still subject to scientific arguments as pointed out in the review papers

(Sarpkaya, 2004; Williamson and Govardhan, 2004) because of the complexity of its dynamics. It should be expected that this complexity dramatically increases in the FIM of multiple cylinders. Flow interference in clusters of cylinders has been the subject of many studies in the past due to practical interests in engineering fields. Two-cylinder systems have been studied the most because they are the simplest multi-cylinder arrangement, and only a few selected references are listed in Table 2.1. Recently, Sumner (2010) reviewed the studies of the flow around two infinite circular cylinders of equal diameter immersed in a steady cross flow. The interference effects strongly depend on the arrangement of the cylinders, flow particulars, and Reynolds number. According to Zdravkovich (1977, 1985, 1987), there could be three kinds of interaction between two cylinders as shown in Figure 2.10:

(a) Proximity interference which occurs when the cylinders are in close proximity to each other.

(b) Wake interference when one cylinder is in the wake of the other.

(c) No-interference when the cylinders are sufficiently apart so that they are almost fluid dynamically independent of each other.

Zdravkovich's classification of the flow regimes is shown in Figure 2.11, and has been widely referenced by other researchers. He divided the flow into five regimes for two stationary cylinders in tandem (1985). For tandem arrangement, Zdravkovich's five regimes are as follows,

(a) Single slender body regime ($d/D<1.1$): The two cylinders behave as a single slender body with a high Strouhal number.

(b) Alternate reattachment regime ($1.1<d/D<1.6$): An alternate reattachment of the shear layers takes place on the front side of the downstream cylinder.

(c) Quasi-steady reattachment regime ($1.6<d/D<2.4$): Quasi-steady reattachment of separated shear layers is observed on the downstream cylinder.

(d) Intermittent shedding regime ($2.4<d/D$): Occasionally, one of the reattachments is disrupted, but there is still no regular vortex shedding behind the front cylinder.

(e) Discontinuous jump (critical spacing): The vortex shedding is intermittently suppressed and replaced by the reattachment flow regime on the front cylinder.

(f) Two vortex streets regime: the vortex streets are formed in the narrow wake behind the front cylinder and in the wide wake behind the downstream cylinder with high and low frequency of vortex shedding, respectively.

Igarashi (1981) and Ljungkrona et al.(1999) experimentally investigated the effect of Reynolds number (Re) on the flow patterns between two stationary cylinders in a tandem arrangement, and the critical spacing in which a discontinuous jump occurs in the measurement in forces or pressure on the downstream cylinder. This discontinuity was observed by many researchers (Zdravkovich, 1977; Igarash, 1981; Alam et al., 2003; Kim et al., 2009). As shown in Figure 2.12, the flow patterns between two stationary cylinders in line depend on both Re and the longitudinal spacing, but is only slightly influenced by the Re in the region of Re>35,000. The critical spacing is also sensitive to changes in Re as shown in Figure 2.13, and its trend closely follows the Reynolds number dependence on the vortex formation length of a single cylinder.

The complexity of flow structures between two stationary cylinders in a staggered configuration is greater than that of two cylinders in a tandem arrangement due to the effect of gap flow and the interaction of four separate free shear layers (Zdravkovich, 1985; Bokaian, 1989; Gu et al., 1999; Gu, 1996; Gu and Sun, 1999; Sumner et al., 2000, 2005; Alam et al., 2005; Alam and Sakamoto, 2005). Sumner et al.(2000) conducted PIV experiments and flow visualization within the low subcritical

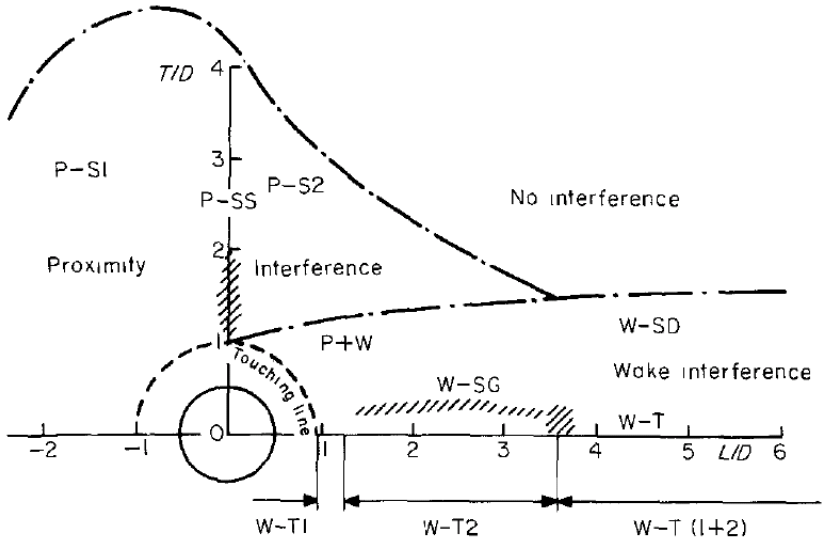

Figure 2.10: Classification of Flow Interference Regime [Reproduced from Zdravkovich 1987]

regime (850<Re<1900), and the general flow patterns for two staggered cylinders are illustrated in Figure 2.14. They found that for even a very small incidence and pitch ratio, the vortex still sheds from the upstream cylinder, which means that VIV can occur for cylinders in close proximity.

As previously discussed, numerous studies on two stationary cylinders in cross flows have been conducted so far. On the other hand, few studies exist on interference between oscillating multiple cylinder systems. For two cylinders, there can be three setups of the cylinders: (a) an elastically mounted cylinder downstream of a stationary one; (b) a elastically mounted cylinder upstream of a stationary one; and (c) two cylinders that are both free to oscillate. When the downstream cylinder is allowed to oscillate behind the upstream one, the downstream cylinder can experience Interference Galloping (Ruscheweyh, 1983), Wake Induced Galloping (Bokaian and Geoola, 1984a) or Wake Induced Vibration (Assi et al., 2006) due to the wake of the upstream one (Bokaian and Geoola, 1984a; Zdravkovich, 1985; Bokaian, 1989; Laneville and Brika, 1999; Brika and Lanveville, 1999; Lam and To, 2003, Kim et al.,

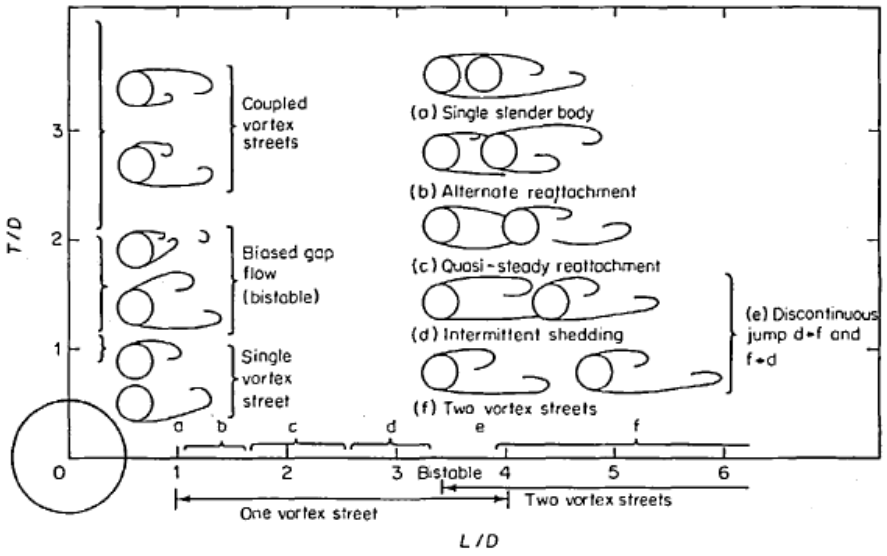

Figure 2.11: Vortex structures in different regimes: L/D is the longitudinal center-to-center spacing ratio [Reproduced from Zdravkovich 1985]

2009, Assi et al., 2006, 2010). Laneville and Brika (1999) conducted tests to examine the effect of a stationary cylinder on the dynamic response of the elastically mounted downstream one. They found that the dynamic response of the downstream cylinder depends on the longitudinal spacing, and the reduced velocity ($U^*=V_r=U/f_{nw}D$) or Re (Assi et al. 2006) as shown in Figure 2.15. The amplitude of oscillation decreases with increasing longitudinal spacing because the vortices generated from the upstream cylinder diffuse more as the spacing increases and, in turn, the lift force also diminishes. (Assi et al. 2010). In addition, Laneville and Brika couldn't observe the hysteresis and intermittent shift in the amplitude response of the downstream cylinder, which were found in the amplitude response of VIV of a single cylinder. Their results demonstrate that the synchronization starts at higher reduced velocity than that of a single cylinder, and the synchronization region is much longer with larger amplitudes. One interesting finding of Laneville and Brika (1999) is that the wake of the upstream cylinder still influenced the response of the downstream one for the longitudinal spacing ratio of 25, even though the tests were done in the wind tunnel. Their findings were commonly observed in other studies.

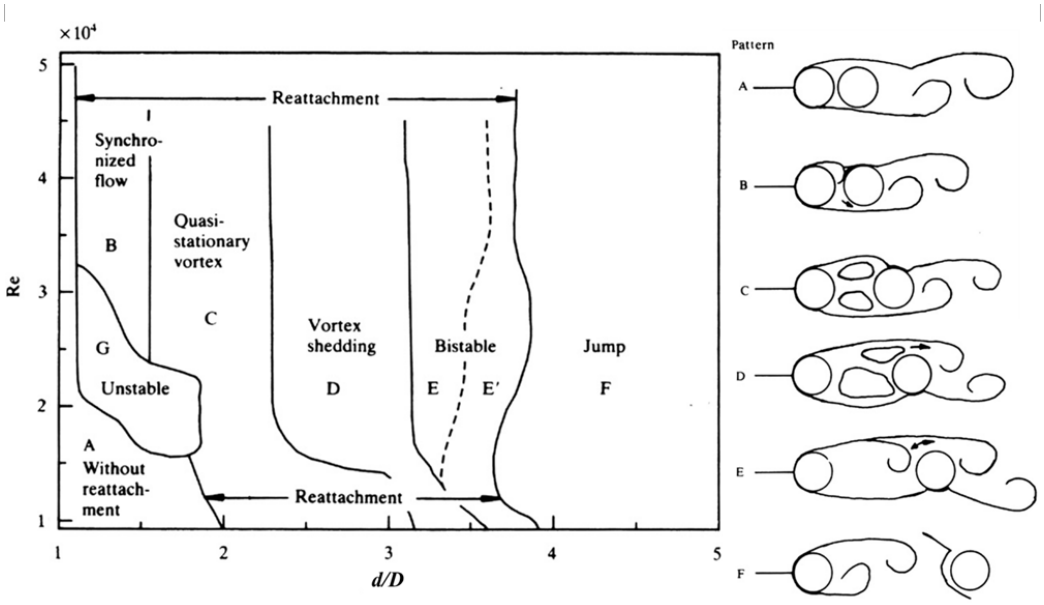

Figure 2.12: Classification of flow patterns for two tandem circular cylinders in cross flow as a function of the longitudinal center-to-center pitch ratio and Reynolds number [Reproduced from Igarashi, 1981]

The mechanism of the oscillation of the downstream cylinder is still being debated because of the complexity in the flow structures between the two cylinders. The flow structures are dependent on Re and the spacing between two cylinders, and continuously change due to the displacement of the oscillating downstream cylinder. King and Johns (1976) explained the response of the downstream cylinder as a type of buffeting because it was caused by the wake interference coming from the upstream one. Bokaian and Geoola (1984a) observed similarities between the response of the downstream cylinder and the classical galloping of a non-circular body, and referred to the phenomena as wake induced galloping. Assi et al.(2006, 2010) were skeptical about the term wake induced galloping because a hydrodynamic restoring force plays an important role in the response of the downstream cylinder in the wake of the upstream one. The restoring force makes the cylinder return to its original position, and this could be considered as the stability of the cylinder rather than instability. They suggested that the phenomenon should be referred to as wake interference vi-

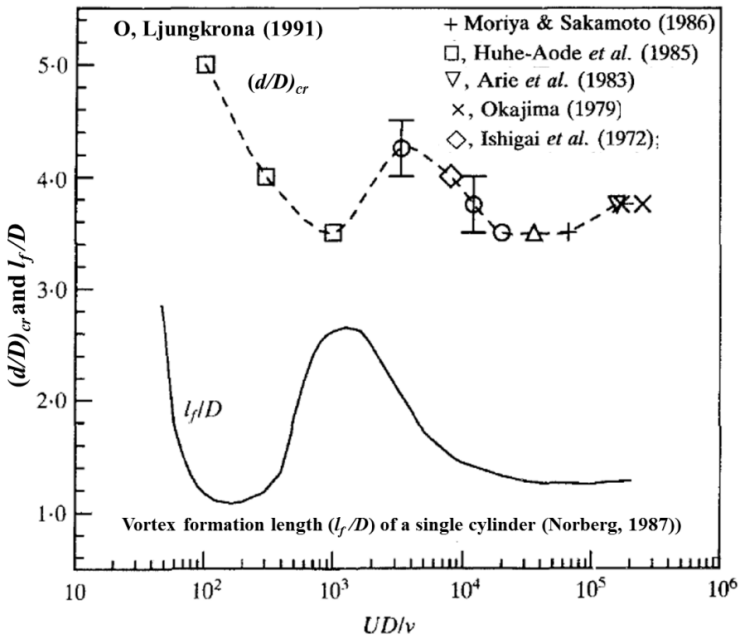

Figure 2.13: Effects of Re on the critical spacing for two stationary circular cylinders in a tandem arrangement, and vortex fromation length of a single cylinder [Reproduced from Ljungkrona et al., 1991]

bration to account for the effect of vortices shed from the upstream cylinder on the lift force acting on the downstream one. They limited the use of this term to only the regime where the unsteady vortex structure interactions between the upstream wake and downstream cylinder cause the oscillation of the downstream cylinder. Assi et al.(2010) conducted experiments to investigate the mechanism of the WIV of the downstream cylinder in the wake of a stationary cylinder. They observed that the oscillatory amplitude continues to increase even though the oscillation frequency passes over the natural frequency of the system. Moreover, by removing upstream shedding vortices in the wake using screens and honeycomb, they investigated the effect of the vortices on the WIV, and found that the downstream cylinder experienced a typical VIV. Based on these observations, they concluded that the WIV is not a resonant phenomenon and a wake dependent type of FIM. They suggested that the wake-displacement mechanism first proposed by Zdravkovich (1977a), as shown in Figure 2.17, could be the most convincing explanation for the WIV, and, at the

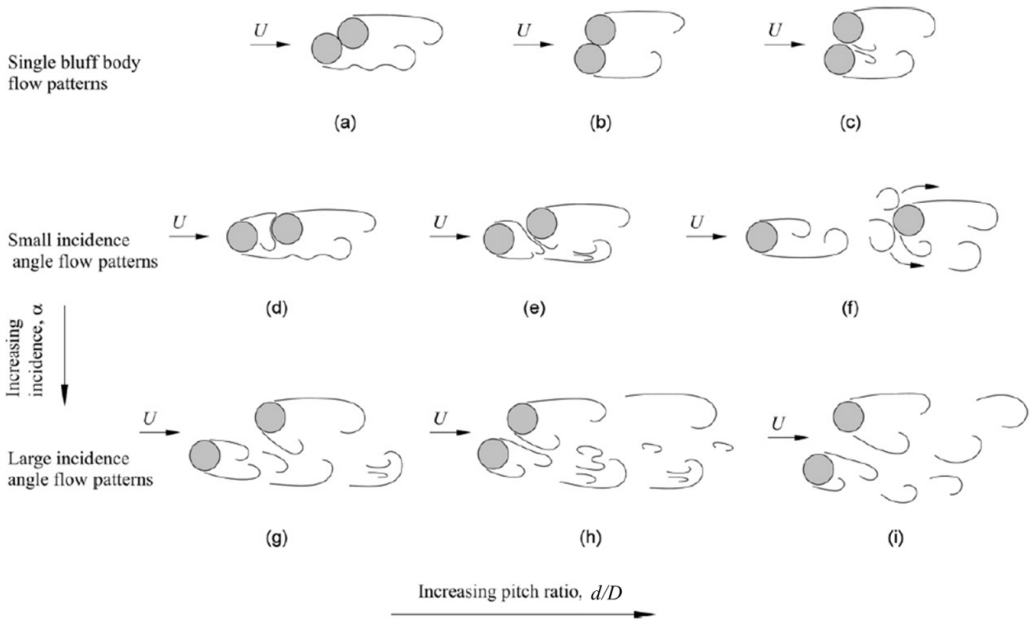

Figure 2.14: Low subcritical regime flow patterns for two staggered circular cylinders in cross-flow [Reproduced from Sumner et al., 2000]

same time, the unsteady vortex-structure plays an important role in sustaining the WIV mechanism as illustrated in Figure 2.16. Even though many efforts have been made to explain theoretically the mechanism of the WIV have been made, there is no completely satisfactory explanation so far (Price, 1995, Assi et al., 2010).

Few previous studies have studied the case of an elastically mounted cylinder upstream of a stationary one. Moriya and Sakamoto (1986) conducted tests with two identical circular cylinders in tandem at Re=65,400. The upstream cylinder was forcibly vibrated in front of the stationary cylinder near the vortex shedding frequency of a stationary cylinder, and the longitudinal center-to-center distance ratio was varied from 2 to 6. They reported that the flow around the two cylinders is synchronized with the oscillation of the upstream cylinder, and the fluctuating pressure on the surface of the downstream cylinder was synchronized with the forced vibration. To and Lam (2007) investigated the response of an elastically mounted cylinder placed upstream of a stationary cylinder, having a twice larger diameter at various positions, and the amplitude response of the upstream cylinder was observed. As shown in

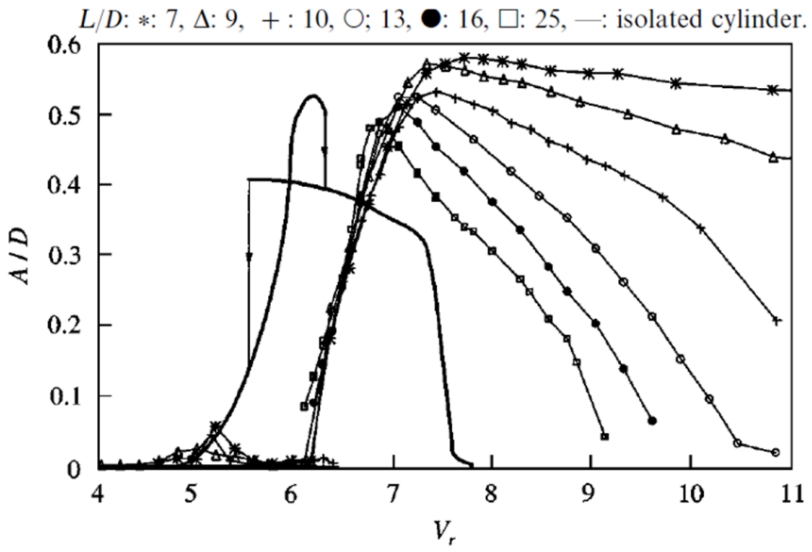

Figure 2.15: Effects of an upstream stationary cylinder on the response of a elastically mounted cylinder at different downstream locations [Reproduced Laneville and Brika, 1999]

Figure 2.18, the oscillation of the upstream cylinder was suppressed at most of the upstream positions, and the lock-in was observed at the reduced velocity near 6. On the other hand, the large amplitude oscillations were observed at a highly reduced velocity (U_R>12) when the upstream cylinder was placed in line with the downstream cylinder at d/D <1.17. From the visualization test, they found that the wake of the upstream cylinder was modified due to the effect of the large downstream one, and thus the vortex shedding frequency was changed. Those results show that the dynamic response of the upstream cylinder is also affected by the presence of the stationary downstream cylinder.

The flow structures of two oscillating cylinders become the most complex among the three possible setups of the two cylinder tests. From the previous experimental studies of the two oscillating cylinders, the conclusions are as follows:

(a) The dynamic response of both cylinders are strongly influenced by the distance between the two cylinders, Re, and free stream turbulence intensity.

(b) For the relatively close tandem spacing, the oscillatory amplitude of the up-

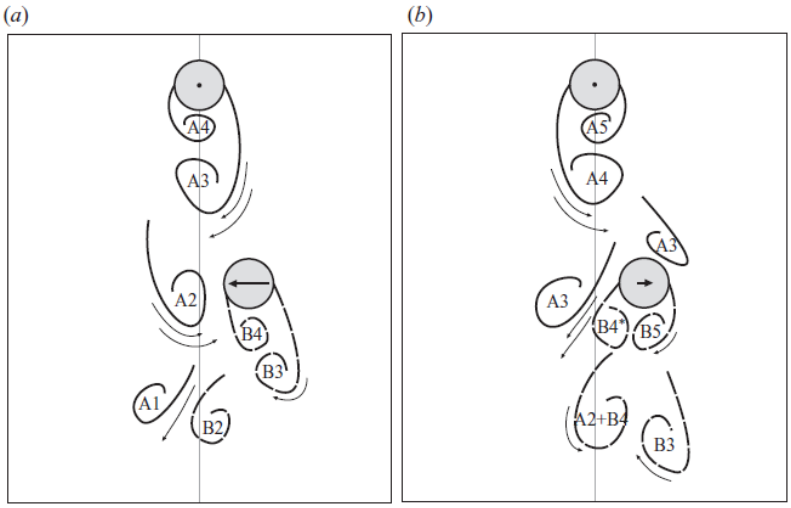

Figure 2.16: Schematic of vortex-structure interaction: (a) enhancing or (d) suppressing the WIV of the downstream cylinder [Reproduced from Assi et al., 2010]

stream cylinder is affected by the oscillation of the downstream cylinder.

(c) For $d/D \approx 20$, the wake of the upstream cylinder still influences the oscillation of the downstream one.

(d) The dynamic response of the downstream cylinder shows similar trends to that of a cylinder in the wake of the stationary cylinder.

(e) In the dynamic response of the downstream cylinder, two or three discontinuities are observed due to the change in the wake structure of the upstream cylinder.

(f) The oscillation amplitude of the downstream cylinder decreases as the downstream cylinder is placed farther away from the upstream one.

(g) The beating phenomenon is observed in the amplitude response of the downstream cylinder.

(h) There is a critical longitudinal spacing at which the fluctuating lift coefficient suddenly jumps, and it is dependent on the test conditions such as the mass-

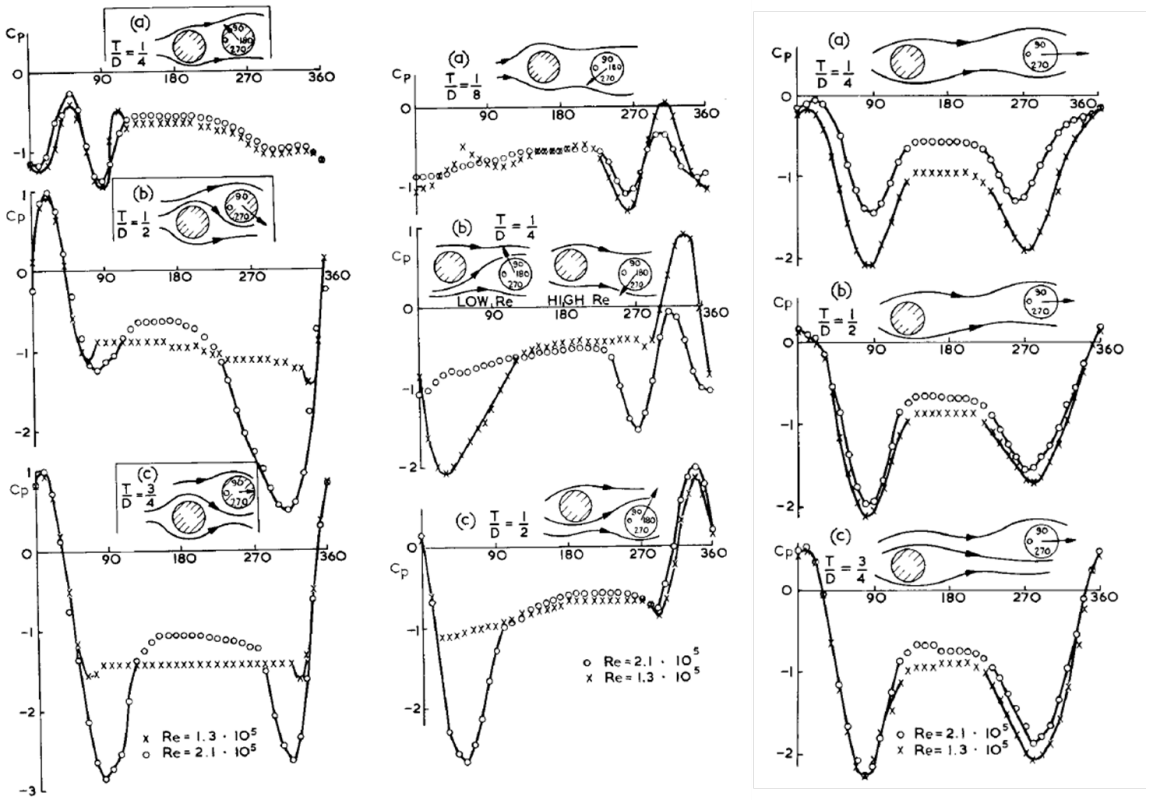

Figure 2.17: Schematic of the wake-displacement mechanism and the measured pressure coefficient around the downstream cylinder: d/D=1.5 (left), d/D=2.0 (center), and d/D=3.0 (right) [Reproduced from Zdravkovich, 1977]

damping ratio, free stream turbulence intensity, and Reynolds number. The critical spacing is usually observed in the region of $3<d/D<4.0$.

(i) For $0.3<d/D<0.5$, the oscillatory amplitude of the upstream cylinder keeps increasing with increases in the free stream velocity.

(j) Both upstream and downstream cylinders oscillate at a lower frequency compared that of a single cylinder in VIV.

Only a limited amount of data exists in the literature for the interference between three and four oscillating cylinders (Hannekamp and Hanmmer, 1981; Igarashi and Suzuki, 1984; Igarashi, 1986, 193; Wang et al., 2002; Liu et al., 2008). Moreover, in

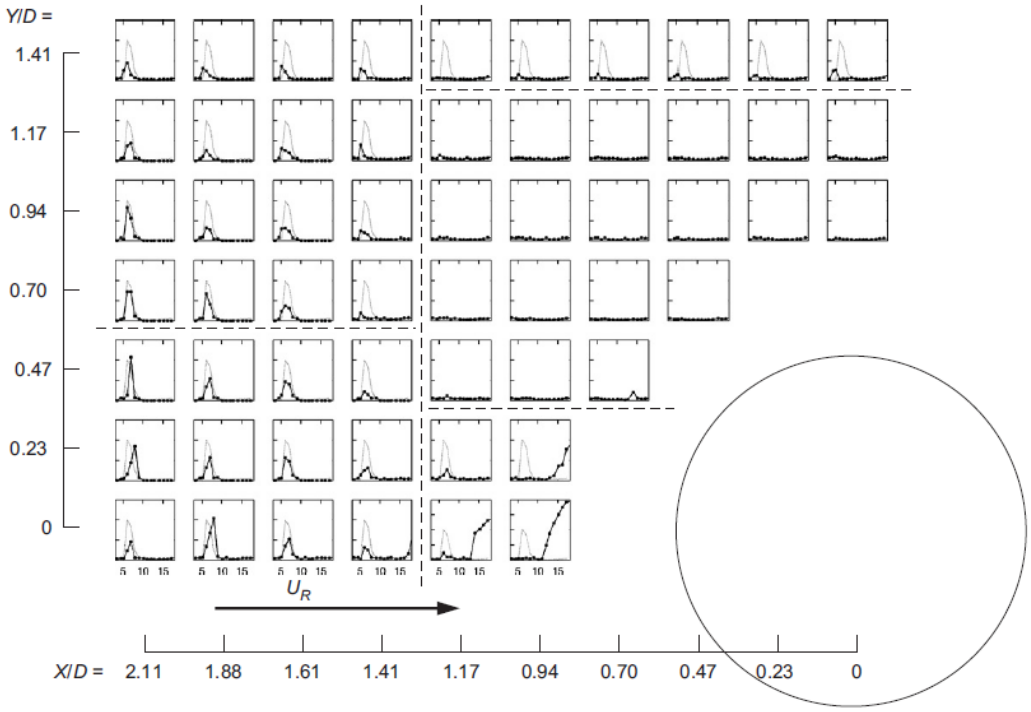

Figure 2.18: Amplitude response of the elastically mounted cylinder placed upstream of a large cylinder at different x, y positions [Reproduced from To and Lam, 2007]

most of the previous studies on three and four cylinders, all cylinders are stationary. It is noteworthy that, in the case of multi-cylinder arrangements, the downstream cylinders are subjected to a high level of turbulence generated from the upstream ones in addition to impingement of shed vortices. All these features add to strong non-linear interactions between cylinders. Hence, the FIM of three or more cylinder-clusters are expected to be more involved and hydrodynamically complex. In this dissertation, the dynamic responses of two, three, and four cylinders, which are all free to oscillate transversely to the flow, are investigated experimentally. The experiments are conducted with variable parameters such as the mass ratio, longitudinal spacing, staggered spacing, spring stiffness, and free stream velocity, to see effects of these parameters on the FIM of multiple cylinders. Additionally, the passive turbulence control is introduced to enhance the FIM of multiple cylinders to harness more energy from the flow. Lastly, some selected research studies are chronologically listed in

Tables 2.1 to 2.4.

Table 2.1: Experimental studies of multiple cylinders in cross flow

Researcher	Years	Num. of Cyl.	Num. of Oscillatory Cyl.	Arrangement TD: (d/D) SG: (h/D)	Re (10^4)	m^*	ζ	Working Fluid	Measurements A/D(max)
King and Johns	1976	2	flexible cylinders	TD1.25-7.0	0.1-2.0	-	-	water	oscillation mode and frequency A/D(0.72), bending moment
Zdravkovich	1977b	2	-	TD1.0-4.0 SG1.0-2.0	2.5-12.0	-	-	air	pressure, reattachment
Okajima	1979	2	-	TD1.07-6.3	4.0-62.0	-	-	air	force, St, separation and reattachment
Igarashi	1981	2	-	TD1.03-5.0	8.7-52.0	-	-	air	pressure, visualization
Hanenkamp and Hammer	1981	2/3/4	all	TD2.0, 3.0, 4.0	0.5-3.0	Sc= 8.5, 19.1		air	A/D, St, pressure
Ruscheweyh	1983	2	2	TD2.3, 4.8, 7.3	0.2-2.0	$m^*\zeta$=1.7, 6.4, 12.8		air	effect of angle of attack A/D, force
Igarashi and Suzuki	1984	3	-	TD1.0-4.0	1.09-3.92	-	-	air	pressure, St, flow patterns, visualization
Zdravkovich	1985	2	2	TD1.0-7.0 SG1.0-3.0	1.0-9.5	-	-	air	A/D, critical reduced velocity
Igarashi	1986	4	-	TD1.0-2.65	0.872-3.92	-	-	air	pressure, St, visualization, flow patterns
Moriya and Sakamoto	1986	2	UP	TD2.0-6.0	6.53	forced		air	A/D, St, pressure
Bokaian	1989	2	DW	TD1.09-2.0 SG0-1.0	0.6	-	-	air	force, modeling

Upstream cylinder(UP), Downstream cylinder(DW), Strouhal number(St), Scruton numbers(Sc)Laser Doppler Anemometry (LDA), Particle Imaging Velocimetry (PIV), Passive Turbulence Control(PTC), Tandem(TD), Staggering(SG), Degree Of Freedom(DOF)

Table 2.2: Experimental studies of multiple cylinders in cross flow (continued)

Researcher	Years	Num. of Cyl.	Num. of Oscillatory Cyl.	Arrangement TD: (d/D) SG: (h/D)	Re (10^4)	m^*	ζ	Working Fluid	Measurements A/D(max)
Hara and Iijima	1989	2	2	TD3.0	~3.25	$m^*\zeta$=0.69,0.83		2 phase flow	effect of air bubbles, A/D, acceleration, visualization
Zdravkovich and Medeiros	1991	2	2	TD1.0-4.0 SG1.1-2.1	0.5-14.0	Sc=10-300		air	effect of damping, A/D, St
Hetz et al.	1991	5	-	TD1.1-1.8	1.2-5.0	-	-	air	St, flow patterns
Ruscheweyh and Dielen	1992	2	DW	TD1.25-2.25	0.05-0.1	forced		water	force, A/D, gap flow switching angle
Igarashi	1993	3	-	TD1.45	4.1	-	-	air	
Wu et al.	1994	2	-	TD3.0-7.0	0.1-4.0	-	-	water/air	St, coherence, visualization,
Mahir and Rockwell	1996	2	2	TD2.5, 5.0	0.016	forced		water	A/D, frequency, visualization
Gu	1996	2	-	TD1.1-3.0 SG1.1-3.5	22.0-45.2	-	-	air	pressure, flow patterns
Lee and Basu	1997	2	-	TD2.0, 3.2	2.4-5.1	-	-	air	pressure, St, velocity field, visualization
Gu and Sun	1999	2	-	TD1.7-2.0 SG0˚-45˚	22.0-39.0	-	-	air	pressure, flow patterns, visualization
Brika and Laneville	1999	2	DW	TD7.0-25.0	0.5-2.7	$m^*\zeta$=0.068		air	A/D, phase angel, St, visualization
Laneville and Brika	1999	2	2	TD10.0-25.0	0.5-3.0	$m^*\zeta$=0.068		air	A/D, phase angel, St, visualization
Summer et al.	2000	2	-	TD1.0-4.0 SG0˚-90˚	0.085-0.19	-	-	water	St, visualization, PIV
Wang et al.	2002	3	-	TD0 SG1.5, 1.6	0.015-0.2	-	-	water	St, visualization

Table 2.3: Experimental studies of multiple cylinders in cross flow (continued)

Researcher	Years	Num. of Cyl.	Num. of Oscillatory Cyl.	Arrangement TD: (d/D) SG: (h/D)	Re (10^4)	m^*	ζ	Working Fluid	Measurements A/D(max)
Lam and To	2003	2	DW	TD0-2.34 SG0-1.41	0.072-0.36	-	0.002	air	A/D, visualization, mean velocity distribution
Lam et al.	2003	4	-	Square bank TD: 1.69-3.83	2.25-5.18	-	-	air	effect of angle of attack, force, St
Alam et al.	2003	2	-	TD6.0	6.5	-	-	air	force, pressure, St, vortex patterns, separation, visualization
Xu and Zhou	2004	2	-	TD1.0-15.0	0.08-4.2	-	-	air	St, visualization
Summer et al.	2005	2	-	TD1.125-4.0 SG0˚-90˚	3.2-7.4	-	-	air	force, St
Alam et al.	2005	2	-	TD0.1-5.0 SG0˚, 10˚	5.5	-	-	air	force, visualization
Alam and Sakamoto	2005	2	-	TD1.1-5.0 SG10˚-75˚	5.5	-	-	air	St, flow pattern
Assi et al.	2006	2	DW	TD2-5.6	3.0-13.0	1.92	0.007	water	A/D(1.4), PIV, visualization
To and Lam	2007	2	UP	TD0-2.11 SG0-2.41	0.054-0.36	-	0.002	air	A/D, visualization
Liu et al.	2008	2/3/4	-	TD2.0-15.0	2.7-8.6	-	-	air	force, St
Alam and Zhou	2008	2	-	TD1.1-5.0	0.65-2.72	-	-	air	force, St, PIV, LDA, visualization
Kim et al.	2009	2	2	TD1.1-4.2	0.44-7.42	Sc= 6.36		air	A/D, flow patterns, visualization
Assi et al.	2010	2	DW	TD4.0-20.0	3.0	2.6	0.007	water	A/D, St, force, PIV
Huera-Huarte and Bearman	2011	2	flexible cylinders	TD2.0-4.0	~1.2	$m^*\zeta$=0.043~1.45		water	2DOF, A/D, St, DPIV

Table 2.4: Experimental studies of multiple cylinders in cross flow (continued)

Researcher	Years	Num. of Cyl.	Num. of Oscillatory Cyl.	Arrangement TD: (d/D) SG: (h/D)	Re (10^4)	m^*	ζ	Working Fluid	Measurements A/D(max)
Present study	2012	2	2	TD2.0-6.0 SG0.5, 1.0	2.8-12.0	1.68	0.017-0.02	water	A/D, oscillation frequency, effect of PTC
Present study	2012	3	3	TD2-5-5.0	2.8-12.0	1.68	0.017-0.02	water	A/D, oscillation frequency, effect of PTC
Present study	2012	4	4	TD2-5-5.0	2.8-12.0	1.68	0.017-0.02	water	A/D, oscillation frequency, effect of PTC
Present study	2013	2	2	TD1.43-4.0	2.36-10.42	0.634-1.662	0.023-0.046	water	A/D, oscillation frequency, effects of PTC and m^*

CHAPTER III

EXPERIMENTAL SETUP

In Part A, all tests are conducted in the LTFSW Channel. The facility, the motion mechanisms, the cylinders, and the passive turbulence control used in this study are described in this section.

3.1 Low Turbulence Free Surface Water Channel

All tests in Part A in this dissertation were conducted in the LTFSW Channel, in the MRELab. The turbulence intensity normalized by the free-stream velocity was reported at 0.095% (Walker, 1996). It enables a continuous flow of water through the test section. The test section is made of plexi-glass and is 2.44 m long, 1.0m wide, and 0.8m deep. The side-walls of the test section are transparent so as to facilitate visualization of the flow past cylinders. The channel re-circulates about 8,000 gallons of water at speed up to 2.0m/sec by an impeller powered by a 20hp induction motor.

3.2 Instrumentation and Data Collection

The cylinder oscillatory displacement is measured using two methods: (i) a Celesco cable extension position transducer (potentiometer) and (ii) through the encoder of the motor/generator in the power take-off system. The voltage measurement is

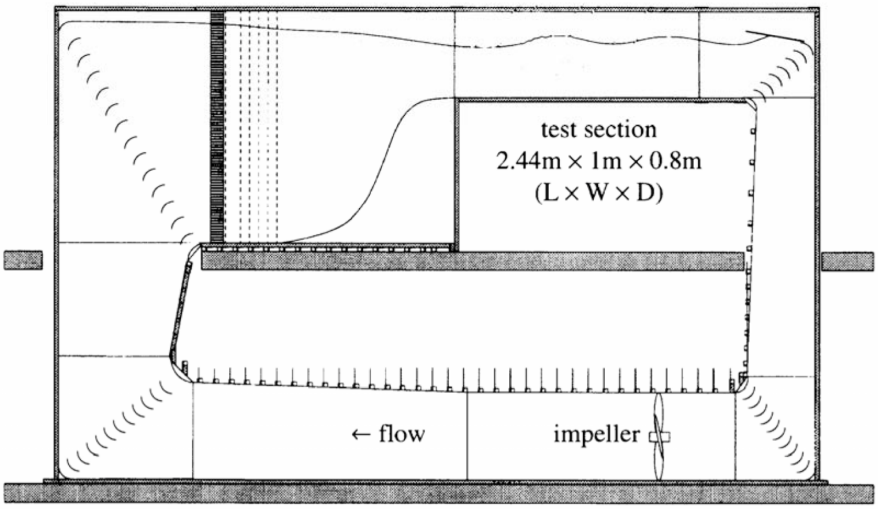

Figure 3.1: Schematic of the LTFSW Channel [Reproduced from Walker et al., 1996]

done by directly connecting the generator to the data acquisition system. The latter consists of a 16-bit analog to digital converter with four-pole, low-pass, Butterworth filters collecting all the data at a 100Hz sampling rate. For each test, after steady state has been reached, 60 seconds of data are recorded. For amplitude plots, the RMS of the 60 largest (positive and negative) amplitude values is calculated. Details regarding the calibration of the LTFSW Channel are given in Bernitsas et al. 2006b [39]. Actual oscillation frequency f_{osc} is calculated by Fast Fourier Transform over the recorded period.

3.3 Oscillators

In order to investigate the FIM on multiple cylinders the 2^{nd} generation of lab prototype of VIVACE was developed and built in 2009. The 2^{nd} generation of VIVACE devices was improved in many aspects compared to the 1^{st} generation. The structure of the new devices is simple but robust, and both real springs and Vck system can be used in the 2^{nd} generation devices. Moreover, the distance between cylinders is adjustable by the rail systems, and they are easy to operate. A simple schematic of

the single-cylinder VIVACE Converter is shown in Figure 3.1. The elements of this module are: a rigid circular cylinder of diameter D and length L, two supporting linear springs each of stiffness $K_{spring}/2$, and damping of the transmission mechanism and $\text{PTO}_{csystem}$. The cylinder is placed with its axis in the z-direction, perpendicular to the flow velocity U, which is in the x-direction. The cylinder oscillates in the y-direction, which is perpendicular to its axis (z-direction) and the flow velocity (x-direction). The four modules of single-cylinder VIVACE Converters are also shown in Figure 3.1. Each device can slide on a rail system to adjust the longitudinal distance between the four cylinders. Vertical distance between the cylinders can be set by spring mounting systems, which are adjustable by 0.25" (0.64cm) increments. Particulars of the four-cylinder VIVACE Converter are listed in Table 3.1. Stiffness of springs and system damping are measured by free decay tests in air. In this paper, real springs and dampers are used rather than the virtual systems used in systematic testing for generation of power envelopes (Lee, 2010; Chang, 2010).

Table 3.1: Particulars of four-cylinders VIVACE Converter

Parameters	Symbol	1st Device	2nd Device	3rd Device	4th Device
Diameter (m)	D	0.089	0.089	0.089	0.089
Length (m]	l	0.914	0.914	0.914	0.914
Oscillating mass (kg)	m	9.53	9.59	9.51	9.58
Spring const. (N/m)	k	744.29	757.41	737.24	747.39
Sys. damping ratio	ζ	0.0206	0.0198	0.0172	0.0168
Damping (Ns/m)	C	3.464	3.382	2.882	2.834
Natural freq. in water	$f_{n,w}$	1.114	1.121	1.109	1.114
Fluid mass displaced by cylinder	m_d	5.671	5.671	5.671	5.671
Mass ratio (m/m_d)	m^*	1.681	1.690	1.677	1.689
Added mass (kg)	m_a	5.671	5.671	5.671	5.671

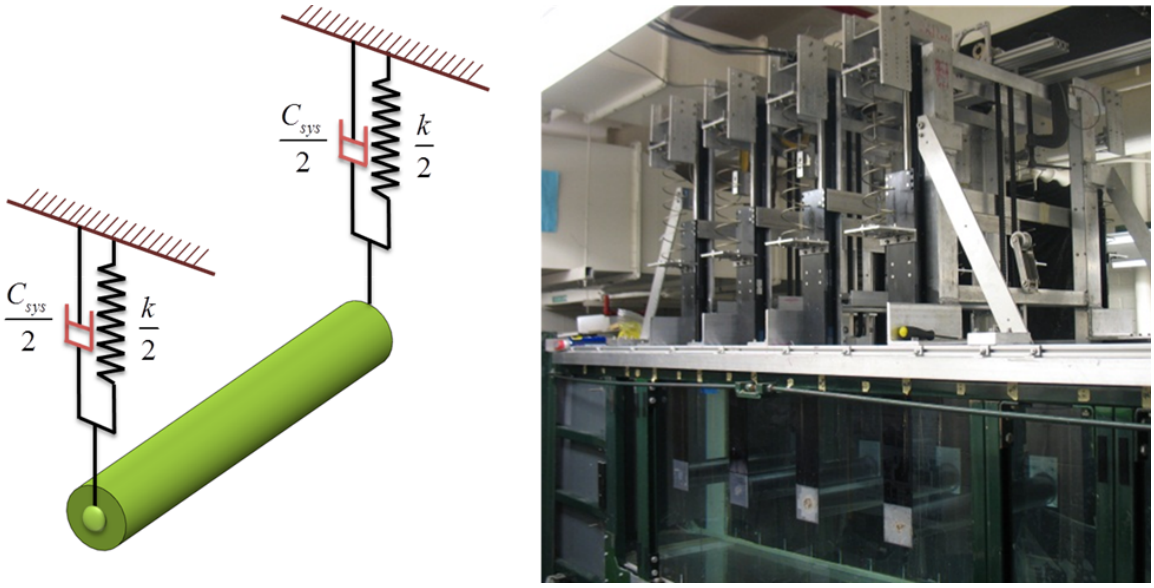

Figure 3.2: Schematic of a single-cylinder VIVACE Converter (left) and four-cylinders VIVACE Converter in the LTFSW Channel (right)

3.4 Passive Turbulence Control

Passive turbulence control (Chang, 2011; Park, 2011) has been studied extensively in the MRELab to alter the FIM of a single cylinder in transverse flow. PTC was studied extensively by Chang et al. (2010 and 2011), and (Chang and Bernitsas 2011) culminating in the development of the *PTC-to-FIM* Map for a single circular cylinder (Park, 2011). Two roughness strips parallel to the cylinder axis are attached running along the entire length of the cylinder. Strip thickness is about equal to the thickness of the boundary layer and affects FIM profoundly. Its width is 0.5" (1.27cm), which covers 16 degrees of the surface of a 3.5" (8.89cm) diameter circular cylinder. PTC is used in this paper to induce synergetic dynamics of multiple cylinders with large amplitude galloping and dramatic expansion of the synchronization range, thus making VIVACE work like a multi-cylinder reciprocating engine. Table 3.2 shows the details of the roughness strip P60 (commercially available) used in the present study.

Table 3.2: Details of roughness strip in PTC

ISO/FEPA Grit designation	Average particle diameter (k)	Thickness of backup paper and tape (p)
P60	$269\mu m$	$578\mu m$
k/D	$(k+p)/D$	Width
$302 \bullet 10^{-5}$	$951 \bullet 10^{-5}$	0.5" (16° for D=3.5")

3.5 Free Decay Test

A VIVACE Converter can be considered a mass-spring-damper system as shown in Figure 3.2. For many vibration systems in engineering problems, damping can be modeled by either as linear viscous damping or as Coulomb damping (Inman, 2001). For the viscous damping system, the damping force is proportional to the velocity of the system, and the system can be considered as a linear system whose responses can be obtained by analytical methods. On the other hand, the Coulomb damping is caused by sliding friction, which introduces nonlinear features into the system, and the responses of the system cannot be analyzed by linear methods. The structural damping of VIVACE is modeled as linear viscous damping, and this model agrees fairly well with physical observations. The cylinder of VIVACE oscillates only transvers to the flow, in the y-direction, and the equation of motion of the linear system is as follows:

$$m\ddot{y} + c\dot{y} + Ky = F \tag{3.1}$$

where m, c, k, and F are the mass of the oscillating parts m including one third of the mass of the two springs, the structural damping coefficient, spring stiffness, and the excitation force. This equation can be written in terms of the natural frequency

in the air, $\omega_n = \sqrt{K/m}$, as

$$\ddot{y} + 2\zeta\omega_n\dot{y} + \omega_n^2 y = f \tag{3.2}$$

where ζ $(=c/(2m\omega_n))$ is the damping ratio. For a free oscillation (no excitation force), the analytical solution of the Eqn. (3.2) is given as,

$$y(t) = Ae^{-\zeta\omega_n t}\sin(\omega_n\sqrt{1-\zeta^2}t + \phi) \tag{3.3}$$

where A is the oscillatory amplitude. The mass and spring stiffness can easily be measured by a static test, but the damping coefficient or damping ratio is a difficult quantity to determine. The damping ratio can be measured by a dynamic test. One approach is the free decay test, which uses the decay envelope of the free response of an under-damped (ζ <1) system. From the Eqn. (3.3), the amplitude of the free oscillation exponentially decreases, and the logarithmic decrement of the amplitude is defined as follows,

$$\delta = \frac{1}{n}\ln\frac{y(t)}{y(t+nT_d} \tag{3.4}$$

where T is the damped period of the oscillation and is defined as follows,

$$T_d = \frac{2\pi}{\omega_n\sqrt{1-\zeta^2}} \tag{3.5}$$

The damped period can be measured from the free decay test, which is the time between successive peaks.

Substitution of the analytical solution and the definition of the damped period given by the Eqns. (3.3) and (3.5), respectively, yields,

$$\delta = \frac{1}{n}\ln\left(\frac{Ae^{-\zeta\omega_n t}\sin(\omega_n\sqrt{1-\zeta^2}t+\phi)}{Ae^{-\zeta\omega_n(t+nT)}\sin(\omega_n\sqrt{1-\zeta^2}(t+nT)+\phi)}\right) = \zeta\omega_n T = \frac{2\pi\zeta}{\sqrt{1-\zeta^2}} \tag{3.6}$$

Solving for this equation for ζ gives,

$$\zeta = \frac{\delta}{\sqrt{4\pi^2 + \delta^2}} \tag{3.7}$$

Measured amplitudes of successive cycles during the free decay test is used to determine the logarithmic decrement as shown in Figure 3.2(a), and then the structural damping ratio can be determined by using Eqn. (3.7). Once the damping ratio and the damped period have been determined from the free decay test, the natural frequency of the system, damping coefficient, and spring stiffness can also be calculated by using their definitions. An example of the free decay test is shown in Figure 3.3, and the simulation result based on the values found from the free decay test is compared with the experimental data. The simulation is in good agreement with the experimental data except for the region of small amplitude oscillations where the nonlinear damping is dominant. For VIVACE tests, the oscillatory amplitude is usually larger than $0.5D$ (4.5cm), so the linear viscous damping model is valid for the VIVACE system. In this dissertation, ten free decay tests were conducted whenever any modification was made to the system, and the averaged values were used to determine the damping ratio and spring stiffness.

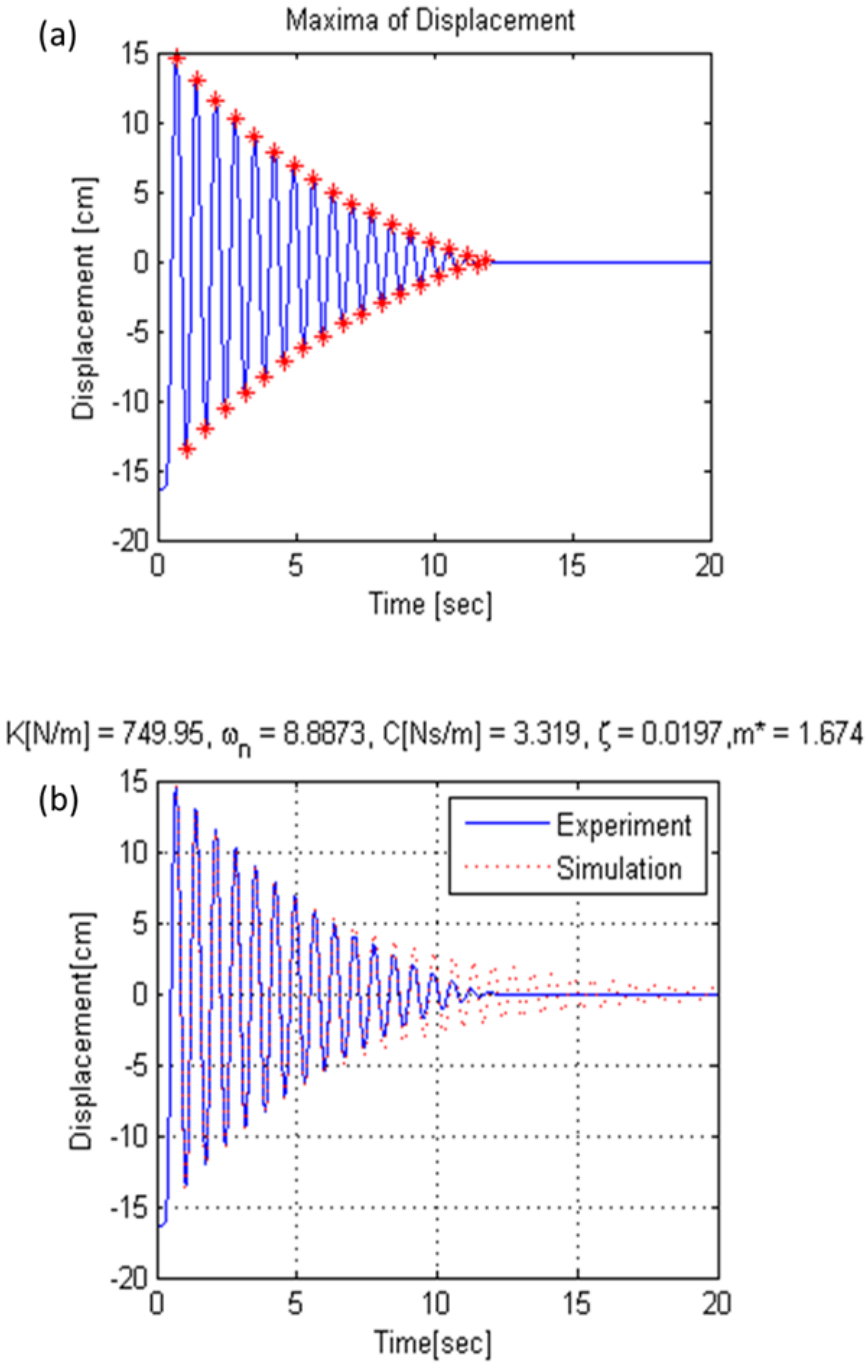

Figure 3.3: An example of an analysis of the free decay tests: (a) displacement response (blue solid) and peaks of oscillatory amplitude (red dot); (b) comparison between the experimental data and simulation results using the estimated spring constant, and damping of the system.

CHAPTER IV

FLOW INDUCED MOTION OF MULTIPLE CYLINDERS

Experiments have been conducted with two, three, and four cylinders with diameter D=3.5" (8.89cm) and length L=36" (91.4cm), with horizontal and vertical distance between centers of cylinders varying from 1.63 to 6 diameters and from 0.5 to 1.0 diameter, respectively. Multi-cylinder systems consisting of two, three, and four cylinders are discussed in this chapter. PTC in the form of roughness strips is used to amplify the FIM of all cylinders in a group. All experiments were conducted in the Reynolds number (Re=UD/ν) range of $28,000 \sim 120,000$. Each oscillator-cylinder system in a VIVACE Converter has slightly different spring stiffness and damping. For the four-cylinder system, two mounting springs are used for each cylinder. In this case, the maximum difference in the spring stiffness among the four cylinder systems is about 2.7%. Variation in damping is about 18.1% among them as shown in Table 3.1. Typical results for two-cylinder, three-cylinder, and four-cylinder configurations are presented in the following sections.

4.1 Effect of Spacing on FIM of Two Smooth Cylinders

Two smooth cylinders arranged in tandem are free to oscillate transversely to the flow. The center-to-center distance d, between the two cylinders is varied from $2.0D$ to $6.0D$. The amplitude response A/D is plotted in Figure 4.1, and compared with A/D of the single smooth cylinder case. The corresponding frequency ratio $f_{osc}/f_n, w$ plots for each cylinder is shown in Figure 4.2. For the upstream cylinder, at all values of the tandem spacing d, response trends are somewhat similar to those of the smooth cylinder but with distinct differences in some cases. For the smallest spacing (d/D=2.0), the trend deviates the most among all the cases, the initial branch being similar to that of the smooth cylinder, the upper branch showing a suppressed amplitude profile with broadened synchronization range, and exhibiting a stronger lower branch. As d/D increases, the response of the upstream cylinder tends closer to that of the single smooth cylinder. It should be noted that the peak amplitudes of the 1st cylinder are increased by up to 7.2% due to the presence of the downstream cylinder for d/D=3.0.

For the second cylinder, the response trends are quite different from those of the single cylinder and the first cylinder for all the tandem spacing values d tested. For d/D=2.0, the initial branch of the second cylinder shows a split-up which is not observed in the single smooth cylinder response or in the upstream cylinder in the two smooth cylinders in tandem. That is, an amplitude bump appears before the upshot of the initial branch occurs at $U^*(=U/f_{n,w}D)\approx$7.0. Furthermore, the upper and lower branches are shifted to higher U^* values with slightly higher amplitude maxima. With increasing d/D, amplitude profiles become more uniform, with a reduced bump size, tending to the smooth cylinder response. Some lose in maximum response amplitude is observed as well. For d/D=2.0, frequency trends of both cylinders also show a deviant response which the oscillation frequency is lower than that of other spacings as shown in Figure 4.2. It is somewhat surprising to notice that, in the

range $5.3<U^*<10.4$, frequencies of both cylinders adhere closely to the frequency of the smooth cylinder with only minor deviations. For $U^*>10.4$, oscillation frequency reduces for both cylinders - compared to the smooth cylinder - particularly at low spacing values.

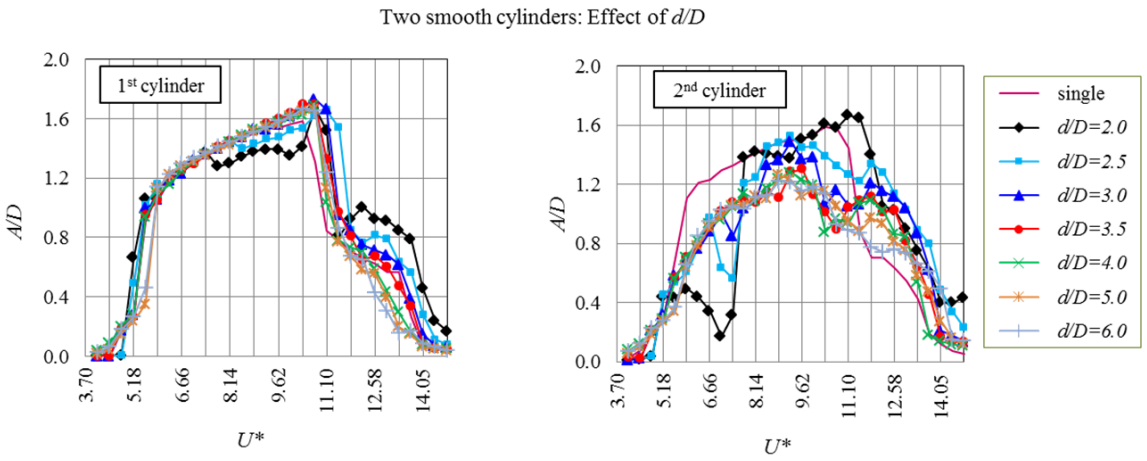

Figure 4.1: A/D of two smooth cylinders in tandem

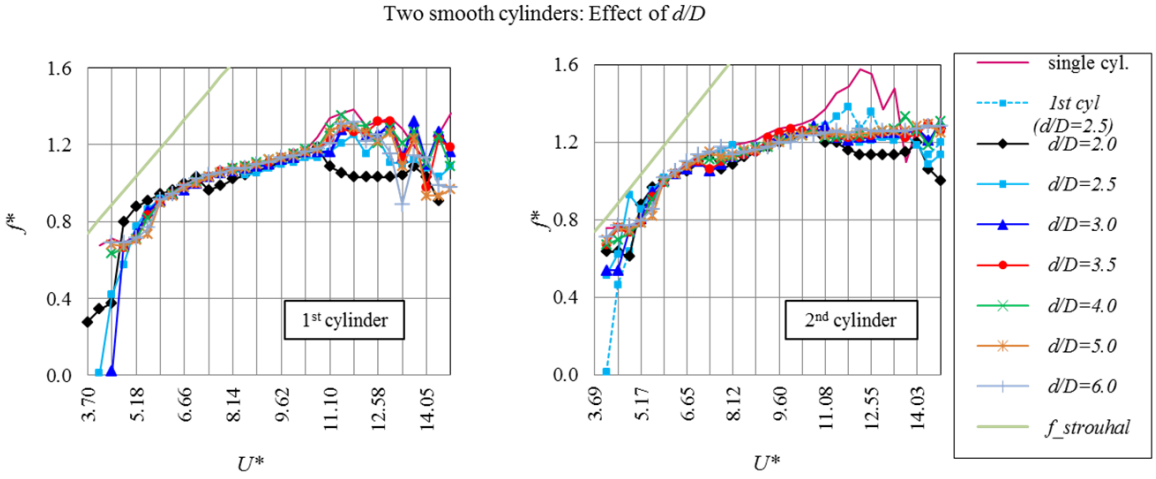

Figure 4.2: $f^*=f_{osc}/f_n$,w of two smooth cylinders in tandem

4.2 Effect of PTC on FIM of Two Cylinders

Two straight roughness strips are attached to the surface of each cylinder symmetrically, one on each side of the cylinder. The angle is measured in degrees from the forward stagnation point in the corresponding ideal flow. Figures 4.3 and 4.4 show the amplitude and frequency response of cylinders in tandem with the PTC. The legend related to P60 (1st cylinder 20°; 2nd cylinder 30°) indicates that sandpaper with roughness P60 is attached starting at 20 degrees symmetrically on both sides of the first cylinder and at 30 degrees symmetrically on both sides of the second cylinder.

With the PTC, the upstream cylinder (1st cylinder) goes into galloping for both strip locations, i.e. 20° and 30°. For the cases with the PTC, amplitude suffers a slight loss of magnitude in the upper branch of VIV compared to the smooth cylinder response. For the P60:30°-30° configuration, results show the maximum drop of amplitude with a more gradual development of the galloping branch for both cylinders. The maximum galloping amplitude of both cylinders is hardly altered by the strip location change.

For the second cylinder (Figure 4.3), up to U^*=10.4, oscillatory trends are similar to those of the second smooth cylinder (Figure 4.1) being characterized by an initial branch, followed by a deep for U^*<7.0 (thus forming a bump). Next, a new initial branch appears followed by a rising upper branch. This behavior, which is also observed in Figures 4.3, 4.5, 4.7, 4.9, and 4.11, is due to the fact illustrated in Figure 4-13. There are two frequencies driving the downstream cylinder one due to the oscillations of the upstream cylinder and one due to its own vortex shedding. In the three cases shown on the right column for the downstream cylinder, the following phenomena occur: (a) For $U^*\approx$6, the two frequencies coincide and the cylinders oscillate nearly in phase. (b) For $U^*\approx$7, the two frequencies differ by a little resulting in small amplitude beating of the downstream cylinder. (c) For $U^*\approx$8, the two fre-

quencies differ appreciably and the second cylinder's own vortex shedding frequency dominates over the frequency of the wake of the upstream cylinder, thus driving the second cylinder.

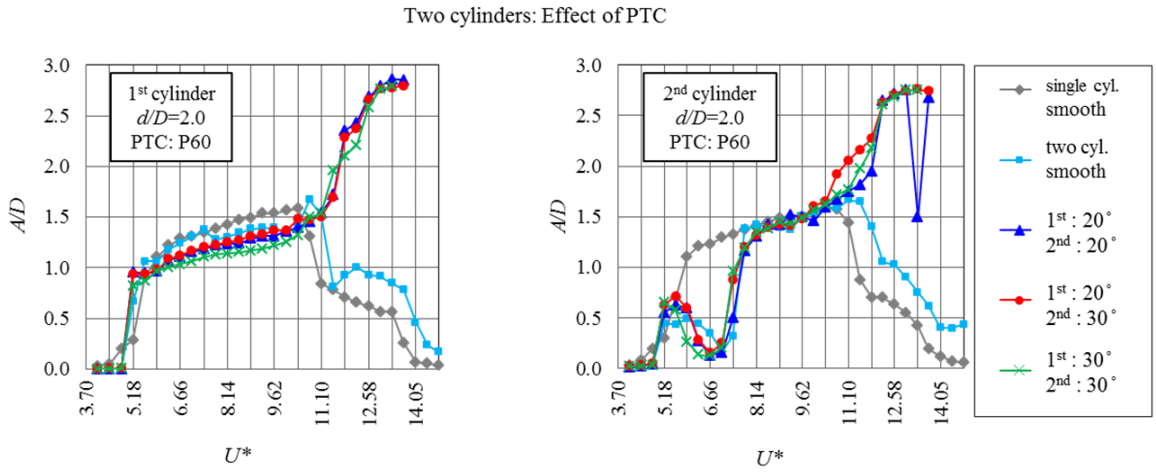

Figure 4.3: A/D of two cylinders in tandem with variable PTC

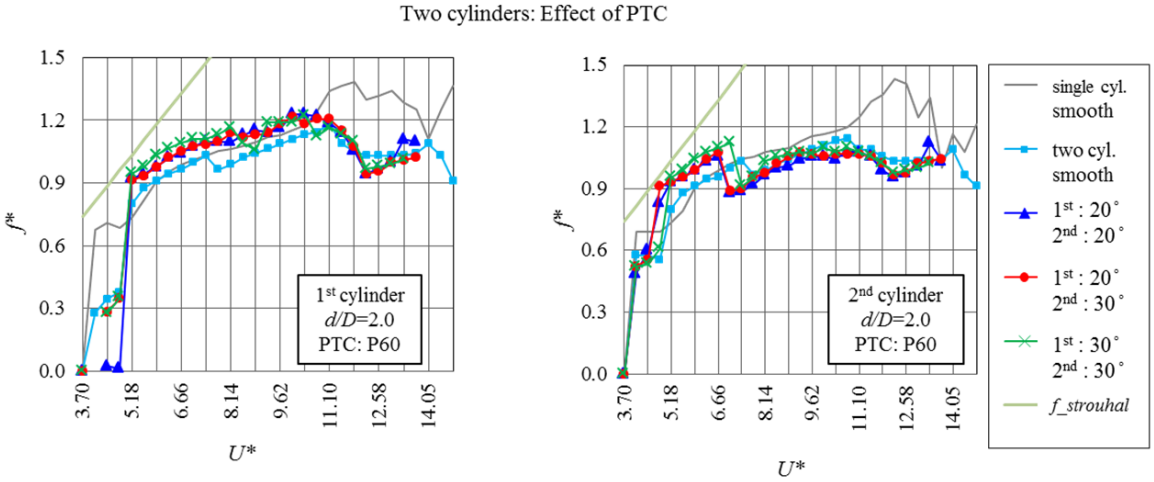

Figure 4.4: $f^*=f_{osc}/f_n$,w of two smooth cylinders in tandem

4.2.1 Conclusion and discussion

For all the roughness configurations, for U^*>10.4, a steep rise in oscillations is observed in Figure 4.3 indicating the onset of galloping. The galloping branch for the upstream cylinder is steeper with slightly higher maxima than those of the downstream cylinder. For the upstream cylinder, at very low U^* values, introduction of the PTC reduces the upstream cylinder oscillation frequency as shown in Figure 4.4. Over a broad range of reduced velocity 4.8<U^*<10.4, oscillation frequencies of the 1st cylinder are only slightly affected by the PTC as shown in Figure 4.4 though some minor effects are observed. The PTC increases the oscillation frequency of the upstream cylinder in the range 4.8<U^*<10.4. For U^*>10.4, the frequency of oscillation shows a sharp decline indicating the onset of galloping. For this higher reduced velocity range (U^*>10.4), the PTC location does not have any notable influence on the oscillation frequency. For both cylinders, frequency declines at the onset of galloping but for the downstream cylinder, frequency decline occurs more gradually compared to the front cylinder. Furthermore, with the PTC, the upper branch (4.8<U^*<10.4) oscillations are faster for the upstream cylinder than the tandem smooth cylinder as shown in Figure 4.4. For the downstream cylinder, results in Figure 4.4 show faster oscillations compared to the downstream smooth cylinder in the tandem two-cylinder case for a short range of reduced velocity up to U^*=7.0. Thereafter, oscillations become slightly slower (lower frequency). Compared to the single smooth cylinder, the oscillation frequency for the downstream cylinder with the PTC is lower for U^*>7.0.

4.3 Effect of Tandem Spacing on FIM of Two Cylinders with PTC

In Figures 4.5 to 4.12, results are presented in a different way than the one used in Figures 4.1 to 4.4. In the latter, no comparisons are made between devices. Results

are discussed for one device at a time. Thus, f_n, w and U^*, which depend on the device's spring and damping parameters shown in Table 3.1 cannot be used. On the other hand, in Figures 4.5 to 4.12, comparisons are made between devices of different properties in the same graph. Thus, the dimensionless quantities $f_n, osc/f_n$,w and U^* cannot be used because the non-dimensionalizing quantities are device dependent. Instead, the actual frequency and Reynolds numbers are used.

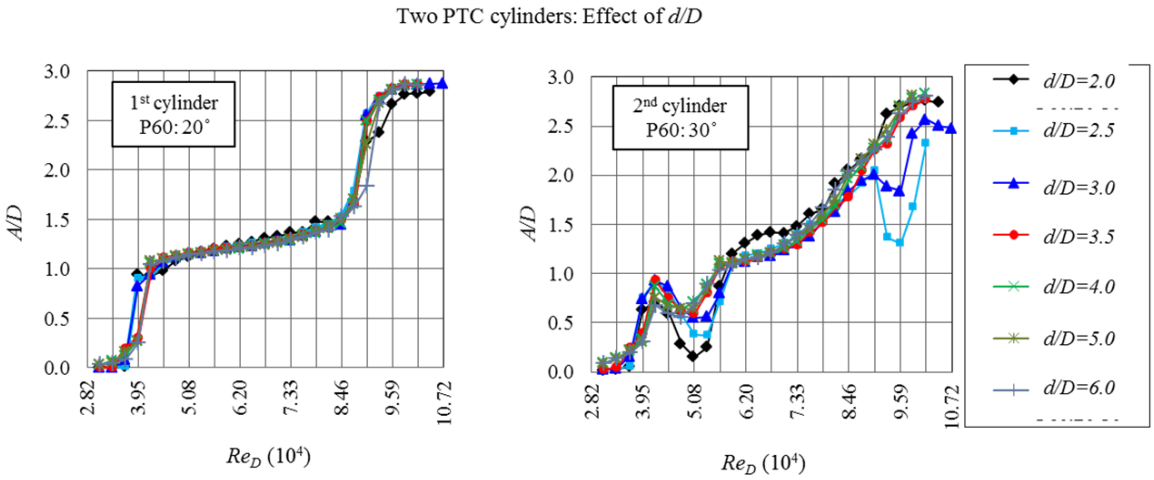

Figure 4.5: A/D of two cylinders with PTC and variable distances

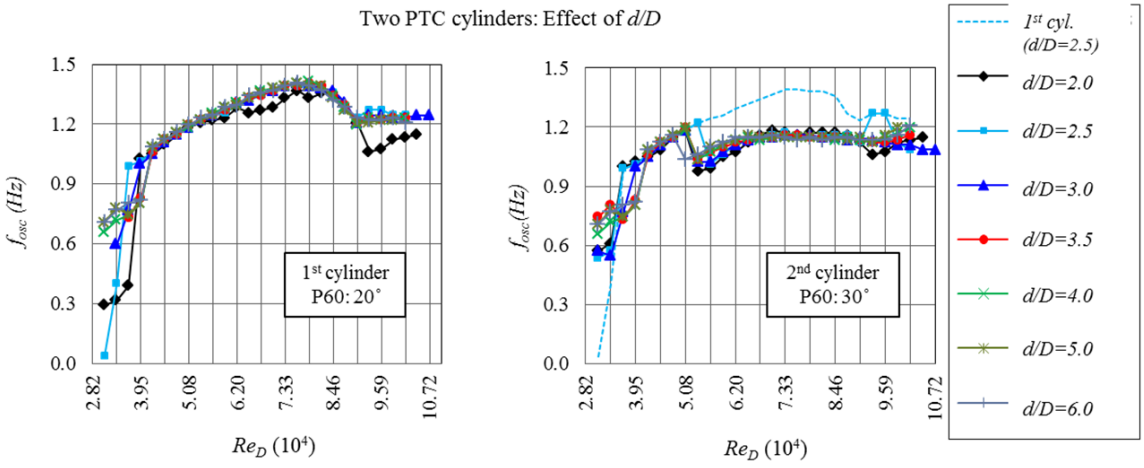

Figure 4.6: f_{osc} of two cylinders with PTC and variable distances

4.3.1 Conclusion and discussion

Based on the previous studies of MREL on the PTC (Chang et al., 2011; Park et al., 2011; Chang and Bernitsas 2011), the type and the positions of the PTC are determined. For investigation of the effect of distance between cylinders with the PTC (P60:20°-30°), d/D is varied from 2.0 to 6.0. Figures 4-5 and 4-6 show the variation of amplitude and frequency response of two cylinders with respect to Reynolds number. For the upstream cylinder, oscillatory trends in A/D and f* are not considerably influenced by the tandem spacing value (Figure 4.5). At d/D=2.0, however, the maximum peak amplitude for the upstream cylinder is slightly lower than the other cases. In all cases, the initial branch is followed by an upper branch, which is then followed by a galloping branch. For the second cylinder (downstream), it is observed that, for d/D>3.0, the VIV upper branch directly merges with the galloping branch with hardly any distinction between them (Figure 4.5). For closer spacing d/D >3.0, however, the galloping branch is distinctly separated from the upper branch. Irrespective of variation in d/D, the amplitude trends for the downstream cylinder share commonalities such as the amplitude bump for U^*<5.36 and a rising amplitude trend in the upper branch. For U^*>6.0, amplitude is maximum for the lowest spacing value. Except for the closest spacing, upstream cylinder frequencies are not affected by d/D over the majority of the U^* range (Figure 4.6). Similar is the case of the downstream cylinder as well but with minor deviations observed at very low and very high Re values (Figure 4.6). Finally, over a broad range of U^*, the oscillation frequency of the first cylinder is higher than that of the rear cylinder (Figure 4.6).

4.4 Effect of Staggering on FIM of Two Cylinders with PTC

In order to investigate the effect of staggering between two cylinders, model tests have been conducted with three different values of vertical center-to-center spacing

h/D, at various d/D values. Only two values of h/D are considered in the present study, 0.5 and 1.0. All tests were conducted for d/D=2.0 for the PTC configuration P60:20°-30°. Amplitude response is shown in Figure 4.7 and frequency response in Figure 4.8.

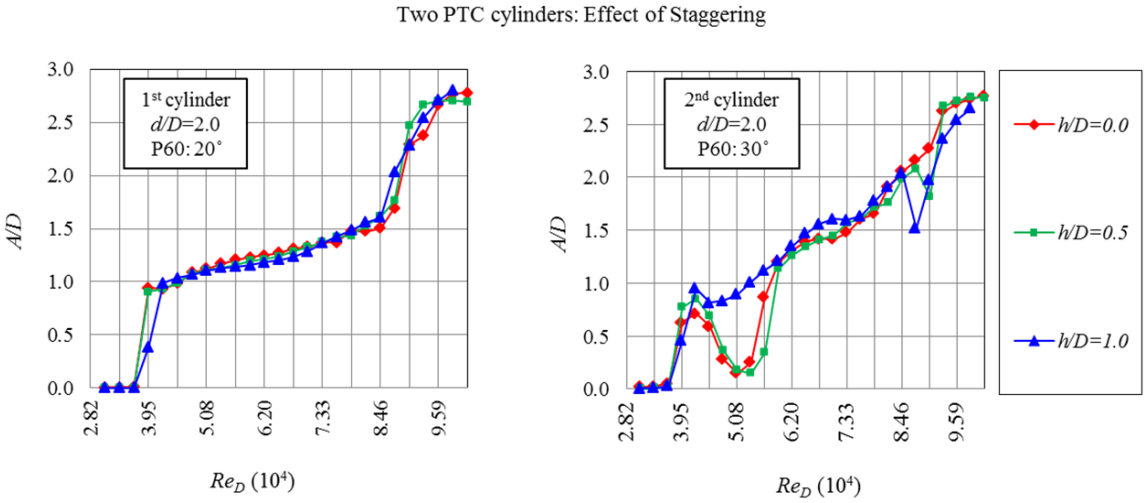

Figure 4.7: A/D of two cylinders with PTC and variable staggerings

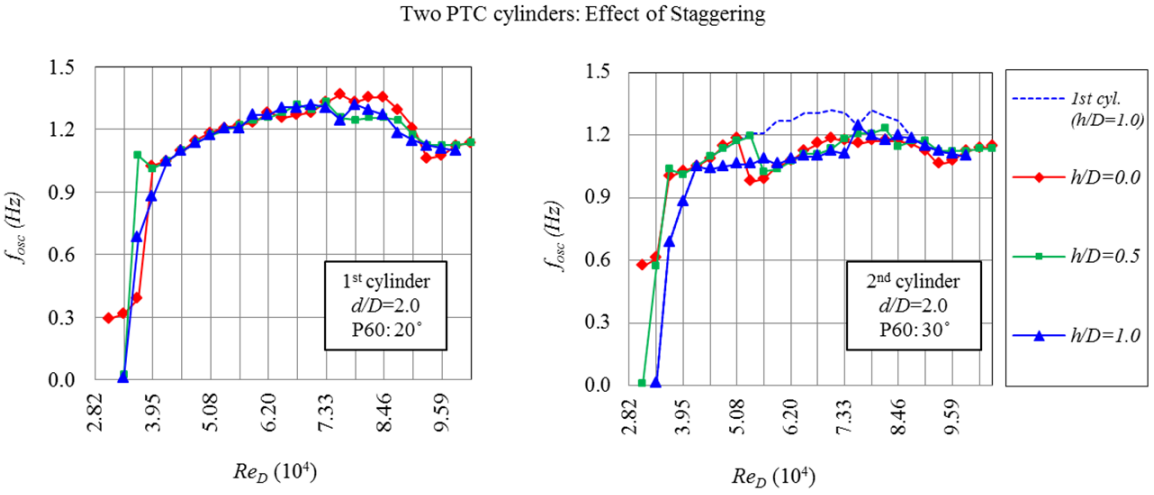

Figure 4.8: f_{osc} two cylinders with PTC and variable staggerings

4.4.1 Conclusion and discussion

When the second cylinder is slightly staggered to h/D=0.5, the front cylinder was found to follow the trend of the h/D=0 case up to U^*≈8.0 followed by a steeper galloping branch thereafter (Figure 4.7). At h/D=1.0, however, the front cylinder exhibits less steep initial and galloping branches compared to the h/D=0 case. Upper branch oscillations are not much affected by the values of cylinder staggering that were tested.

The second cylinder oscillations exhibit the trend previously noted (e.g., as in Figure 4.5) for h/D=0.5. For h/D=1.0, the initial bump has substantially reduced with the upper branch almost directly following the initial branch (Figure 4.7). Higher staggering h/D values bring greater separation between the VIV and galloping branches for the downstream cylinder. For the tandem case h/D=0, the VIV upper branch collapses onto the galloping branch without significant demarcation between them. Higher h/D values also bring a slopping galloping branch with slightly lower amplitude maxima for the rear cylinder (Figure 4.7).

4.5 Flow Induced Motion of Three and Four Cylinders with PTC

Besides tests with two cylinders, model tests have been carried out with three and four cylinders and varying d/D. Results of tests with three cylinders are shown in Figures 4.9 and 4.10 and those with four cylinders are shown in Figures 4.11 and 4.12. It is pointed out that the results with three and four cylinders are very similar for the three upstream cylinders. Specifically, the three upstream cylinders were hardly affected by the presence of the fourth downstream cylinder for d/D>2.5. The results of tests both with three and four cylinders are presented at the same time due to their similarities. For all cases presented here, all cylinders are placed in tandem

configuration. In all these tests, the longitudinal center-to-center distances between cylinders are kept equal and the PTC is applied symmetrically on cylinders at 30° from the front stagnation point of the corresponding ideal flow. The system parameters are presented in Tables 3.1 and 3.2 As seen in Table 3.1, the four oscillators have slightly different stiffness and damping characteristics. Only cylinders with the PTC are considered, because the PTC promotes high-amplitude oscillations (galloping) and expands the range of synchronization by a factor of 2−3 by achieving back-to-back VIV and galloping. These results in dramatic increase in the operational envelop of the VIVACE Converter (Lee and Bernitsas, 2011; Chang and Bernitsas, 2011). Testing was conducted on three and four-cylinder systems with the PTC (P60; starting at 30° for all four cylinders), d/D varying from 2.5 to 5.0. Amplitude and frequency measurements are shown in Figures 4.9 to 4.12. Results are presented so that the effect of d/D for each cylinder can be brought to light.

4.5.1 Conclusion and discussion

4.5.1.1 Amplitude Response of Three and Four Cylinders with PTC

First, the amplitude response of each cylinder for both tests with three cylinders and four cylinders is discussed at the same time, followed by discussion of the frequency response.

First cylinder *A/D*

In Figures 4.9 and 4.11 the upstream-most cylinder is referred to as 1st cylinder. The presence of the other downstream cylinders practically does not affect the oscillations of the 1st cylinder irrespective of the d/D value. In all cases, the 1st cylinder experiences VIV followed by galloping oscillations with peak amplitude nearly the same. The galloping branch has two sub-branches: (a) a steep branch followed by (b) a sloping branch in all the cases. The maximum amplitude for d/D>3.0 is slightly

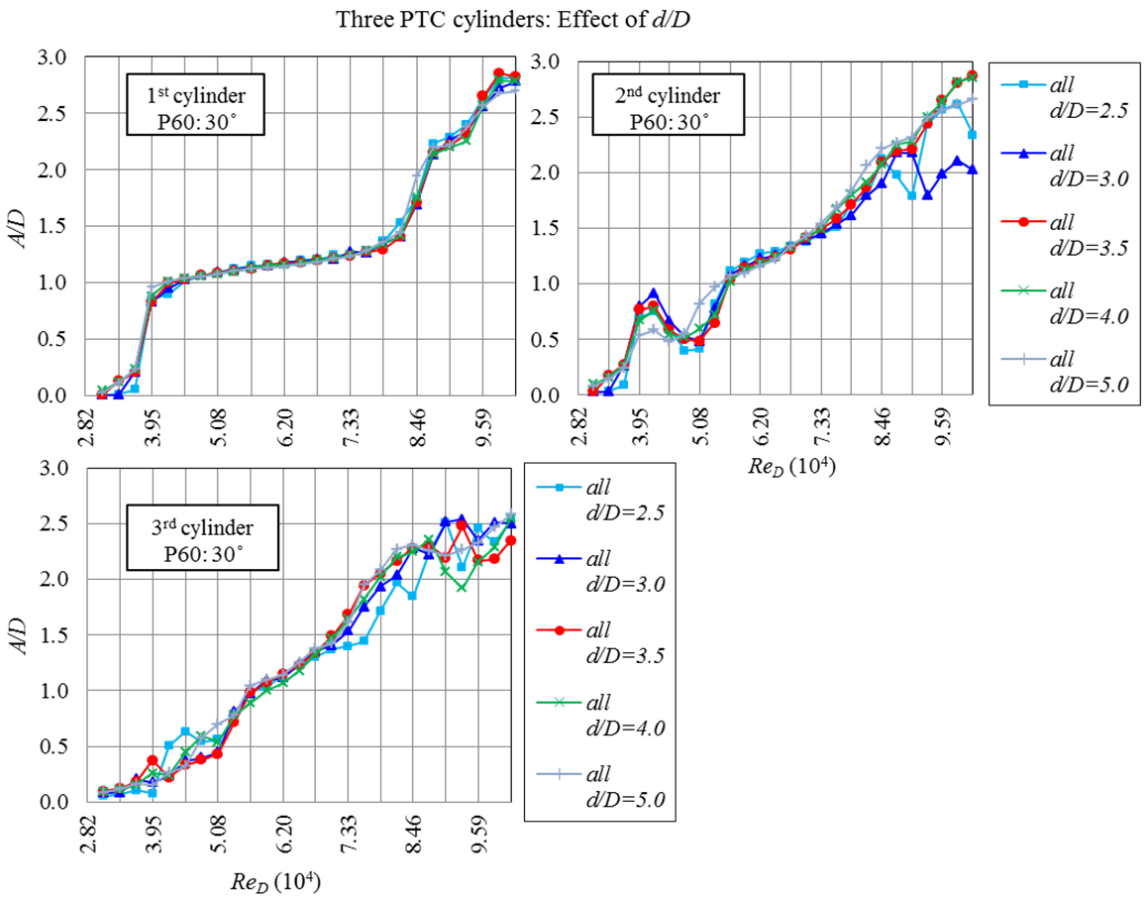

Figure 4.9: A/D of three cylinders with PTC in tandem

greater than that of smaller d/D values ($d/D \leq 3.0$). An overall maximum of $A/D \approx 2.9$ is reached during galloping.

Second cylinder *A/D*

The initial amplitude bump smoothens out as d/D increases as Figures 4.9 and 4.11 show for the second cylinder. In the upper branch, oscillations are not seriously affected by d/D except that the branch becomes slightly steeper with larger d/D. At higher Re ($Re > 8.74 \times 10^4$), cylinder tends to gallop at all values of d/D but more predominantly for higher spacing ratio, $d/D=4.0$. For $Re > 8.74 \times 10^4$, however, response does not follow any specific trend with respect to d/D though the maximum peak amplitude is the highest for $d/D=4.0$. This indicates that the fluid dynamic response

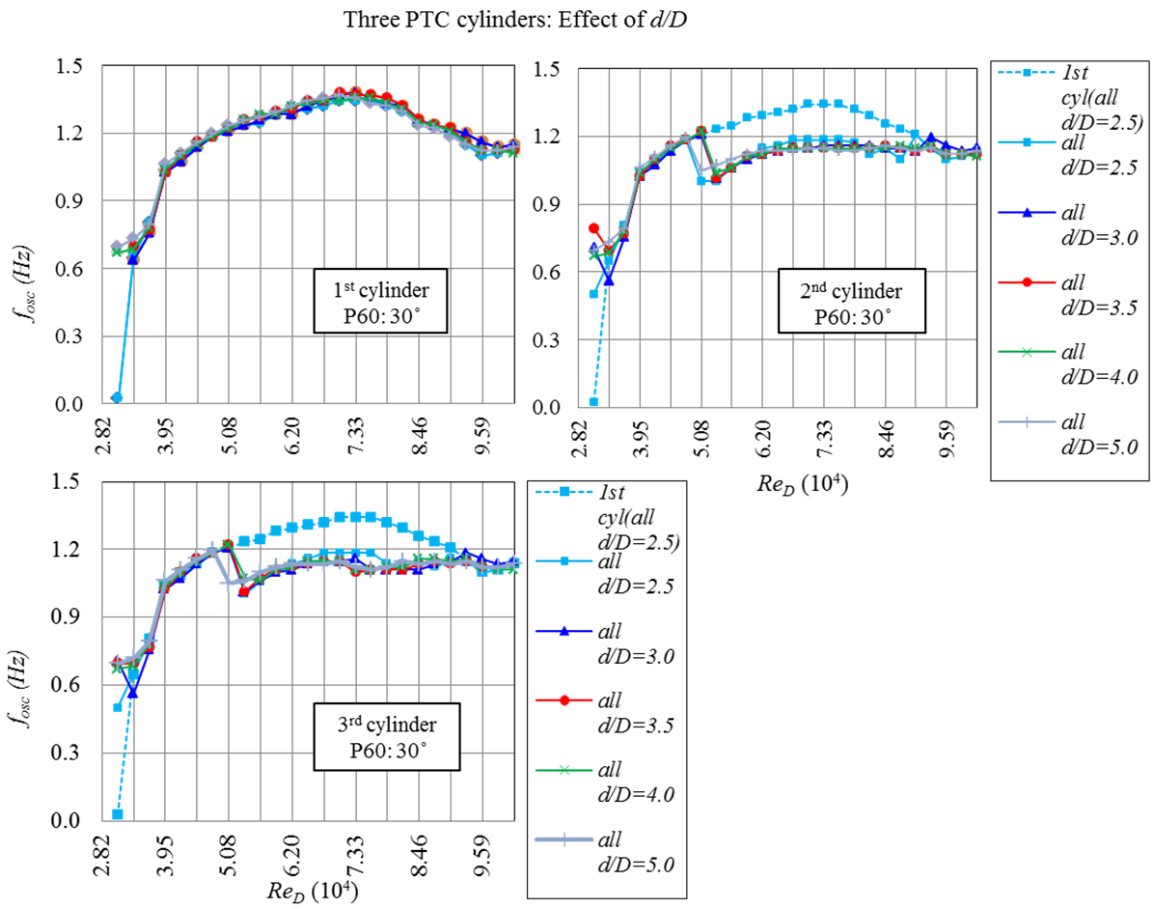

Figure 4.10: f_{osc} of three cylinders with PTC in tandem

of the system with respect to the inter-cylinder spacing is significantly non-linear at higher reduced velocities

Third cylinder *A/D*

With the exception of d/D=2.5, for all other spacing ratios, oscillatory characteristics of the initial and upper branches are closely identical neglecting minor deviations as Figures 4.9 and 4.11 show for the third cylinder. In fact, a clear distinction between initial branch and upper branch is not observed except for d/D=2.5. For Re>8.74×10^4, cylinder tends to gallop but with only reduced maximum peak amplitude compared to the first and second cylinders. It should be noted though, that maximum amplitude of A/D=2.5 is still reached. Further, the multi-cylinder system

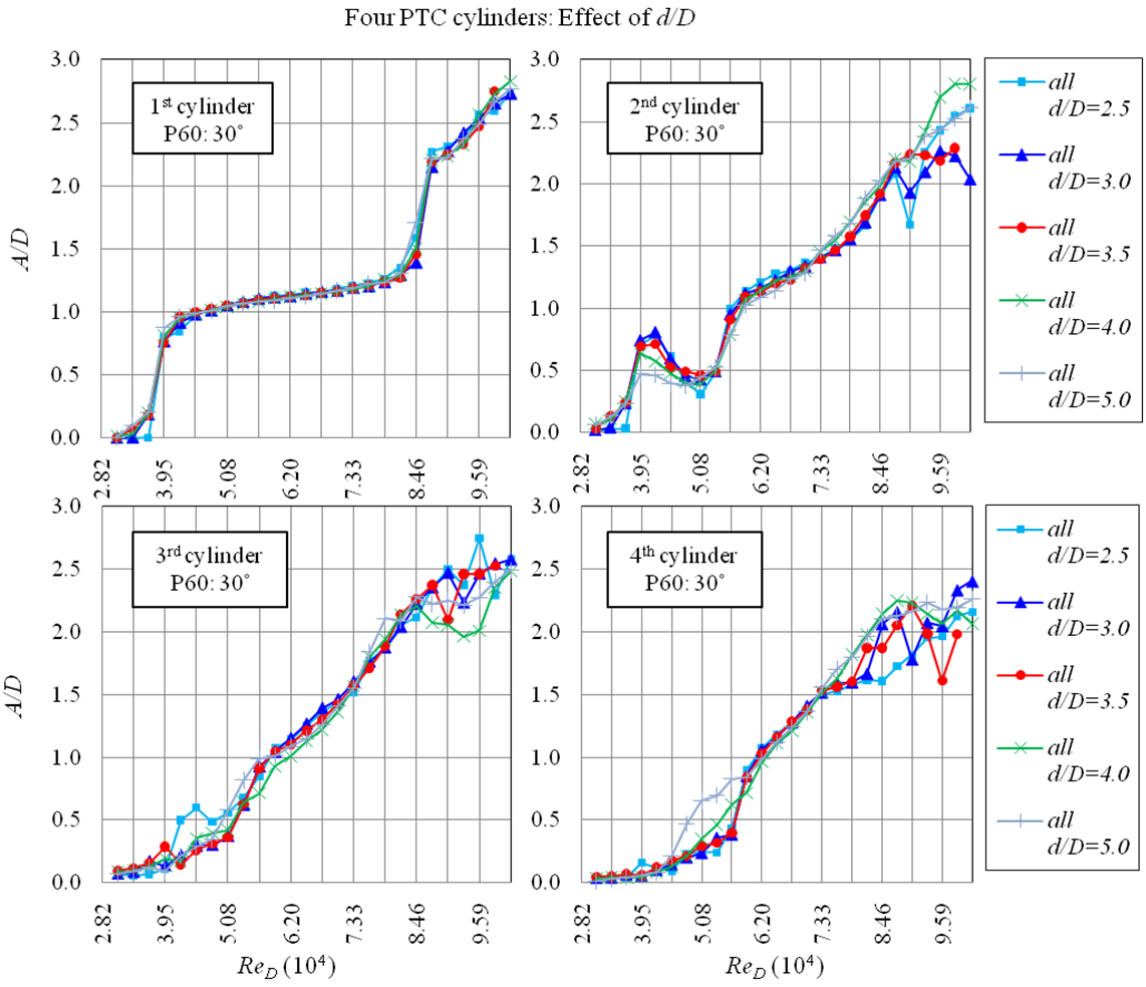

Figure 4.11: A/D of four cylinders with PTC in tandem

extracts so much hydrokinetic energy from the fluid flow that a significant drop in free-surface level occurs between the first and the downstream-most cylinders. Consequently, the third and fourth cylinder responses are subject to stronger free-surface effects that the first two cylinders. As the velocity increases, so does the response amplitude, making the cylinders reach closer to the free-surface and resulting in the strong fluctuations the graphs exhibit for Re>8.74×10^4.

Fourth cylinder *A/D*

This kind of oscillatory behavior is observed for the fourth cylinder as well, as Figure 4.11 shows for the fourth cylinder. Apart from stronger free-surface effects,

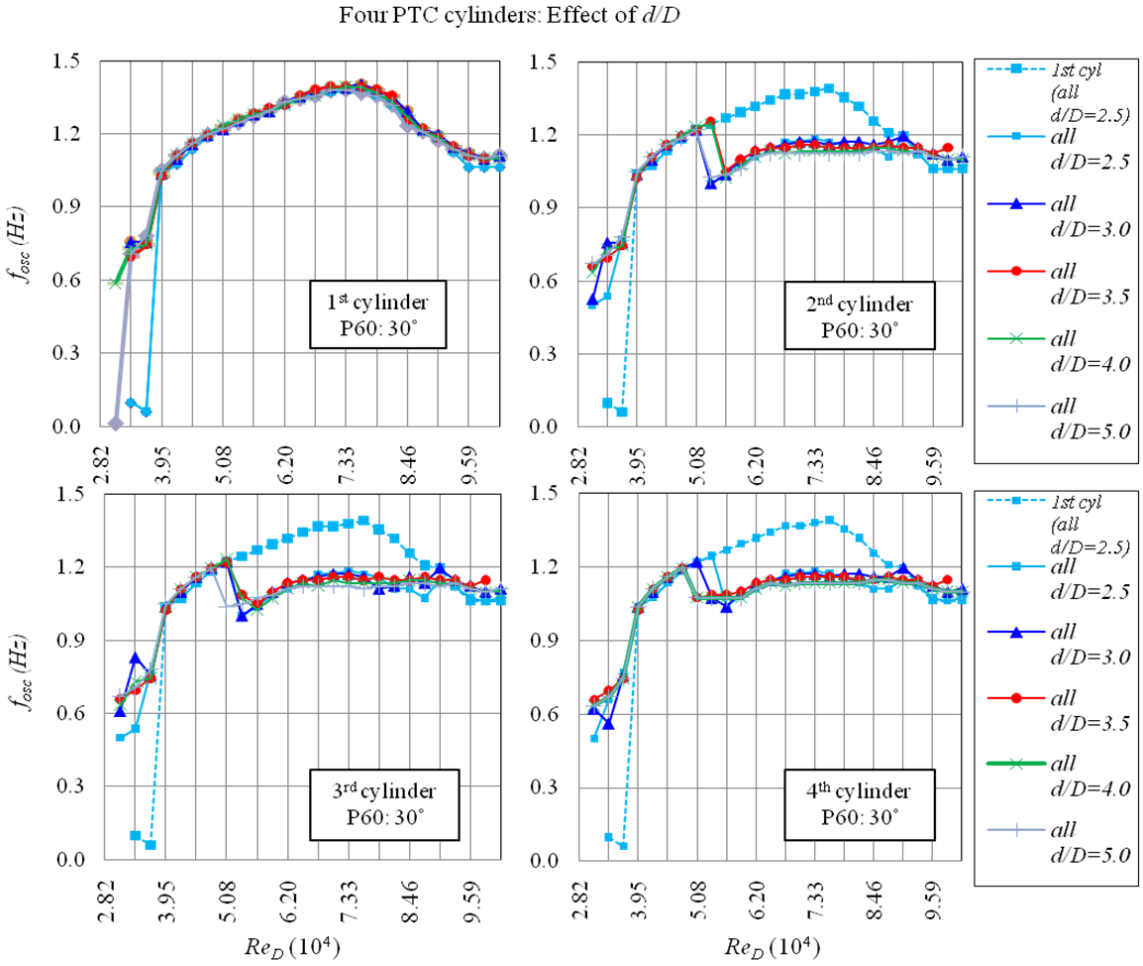

Figure 4.12: f_{osc} of four cylinders with PTC in tandem

to which the downstream stream most cylinder is subjected, a peak amplitude of about A/D=2.4 is obtained for the fourth cylinder for d/D=3.0. Overall, it is inferred that the farther downstream the cylinder is the stronger are the free-surface effects and the more suppressed the peak amplitude of galloping is. In spite of these most adverse conditions, an $A/D\approx$2.4 is still maintained by the fourth cylinder. It should be noted that one of the characteristics of galloping is the continuous increase of amplitude with increasing velocity until system failure or limits are reached. In this case the free-surface limit is reached. Of course, in this complex flow, in the TrSL3 regime [44] with four bodies and with turbulence stimulation, several factors are unknown and have never been studied before. Besides the free-surface effects,

such factors include: (a) The PTC, which may trigger transition to turbulent flow. (b) The higher turbulence of the incident flow marked with significant fluctuations leading to a very complex interaction between the cylinder motion and the incident flow. (c) The strong interaction of downstream cylinder boundary layer with wakes from the upstream cylinders resulting in generation and dissipation of vorticity from the cylinder and consequent amplitudes of excitation. These issues are being considered in the MRELab as part of the research in support of the VIVACE Converter development.

4.5.1.2 Frequency Response of Three and Four Cylinders with PTC

As Figures 4.10 and 4.12 show, frequency response of the 1st cylinder shows that d/D is least influenced among the four cylinders over the Reynolds number range of 2.80×10^4 to 1.20×10^5. For the downstream cylinders, oscillation frequency is notably affected by d/D ratio (Figure 4.10). Predominant influence of d/D could be seen in the short range of $5.0\times10^4<\text{Re}<6.0\times10^4$ after the commencement of oscillations. Over the remaining range of Re, the effect of d/D on the response frequency is not significant. For all cylinders and for all d/D ratios, for $\text{Re}>8.74\times10^4$, a decline of oscillation frequency is observed indicating galloping is also observed in two-cylinder configurations.

4.6 Main findings

Several observations were made based on the test results throughout this chapter. The major findings are summarized below.

- For two smooth cylinders in tandem, in-flow spacing significantly influences the downstream cylinder. The upstream cylinder is affected less. Even in the absence of galloping, both cylinders reach A/D=1.75. Frequency variation of

the first cylinder is smoother than for the second cylinder.

- For two cylinders with the PTC, both cylinders exhibit amplitudes up to (2.8-2.9)D in galloping for reduced velocity U^*>10. The downstream cylinder experiences a drop of amplitude to 0.2D for 5< U^*<7.5. Both cylinders achieve back-to-back VIV and galloping increasing the range of synchronization and consequently the power envelop of hydrokinetic energy conversion.

- For the two-cylinder PTC system, the upstream cylinder amplitude reaches 2.9D (Channel limit) for all values of cylinder spacing. The downstream-cylinder amplitude also reaches 2.8×10^4 but varies with in-flow inter-cylinder spacing and drops over short ranges of U^*.

- For two cylinders with the PTC, cylinder staggering changes the second cylinder oscillations while the upstream cylinder is mildly affected. Cylinder staggering enhances high-galloping motions at high U^*.

- For three and four cylinders with the PTC, the upstream cylinder is hardly affected. All other cylinder response changes with spacing. All cylinders achieve back-to-back VIV and galloping reaching maximum amplitudes of (2.2-2.8)D resulting in such high power-density that drop in free-surface level is forced.

- The high responses of all four cylinders in the four-cylinder systems considered in the current study are attributed primarily to the wake-boundary layer interaction phenomenon. Gap flow occurring between cylinders is also an important factor.

- PTC makes it possible to bring cylinders to close proximity and have them work synergistically making the VIVACE Converter a real three-dimensional device; an important step toward operating like fish in dense school formations. This results in high power harnessing density (Chang and Bernitsas, 2011).